PAPER

Check for updates

Superflexible C$_{68}$-graphyne as a promising anode material for lithium-ion batteries†

Bozhao Wu, [ID] [a] Xiangzheng Jia, [a] Yanlei Wang, [ID] [b] Jinxi Hu, [a] Enlai Gao [ID] *[a] and Ze Liu [ID] *[a]

The breakthrough in the synthesis of graphyne, graphdiyne and graph-4-yne stimulates interest in studying new members of the graphyne family for promising applications. In this work, a new allotrope of graphyne with excellent stability and an ultrahigh specific surface area of 4255 m^2 g^{-1}, named C$_{68}$-graphyne, is predicted by first principles calculations. Mechanical tests reveal that C$_{68}$-graphyne exhibits much smaller in-plane tensile stiffness ($\sim$50.5 N m^{-1}) and out-of-plane bending stiffness ($\sim$0.5 eV) than graphene (in-plane tensile stiffness 350 N m^{-1} and out-of-plane bending stiffness 1.4 eV), suggesting C$_{68}$-graphyne as a superflexible material. Meanwhile, our results show that monolayer C$_{68}$-graphyne is a semiconductor with a direct band gap of 1.0 eV, which can be tuned by strain-engineering, and the calculated carrier mobility is as high as 1.81 $\times$ 10^5 to 2.97 $\times$ 10^5 cm^2 V^{-1} s^{-1} at 300 K. Finally, the potential application of C$_{68}$-graphyne as an anode material for lithium-ion batteries is explored and predicted. The calculated results show highly efficient charge transfer from the adsorbed Li ions to C$_{68}$-graphyne yet a low diffusion barrier for Li ions in C$_{68}$-graphyne for fast charge/discharge rates. The storage capacities for Li in monolayer and bilayer C$_{68}$-graphyne are calculated to be as high as 1954 and 1675 mA h g^{-1}, respectively. These features make C$_{68}$-graphyne a promising anode material for lithium-ion batteries with excellent energy storage capacities as well as fast charge/discharge rates.

1. Introduction

Carbon has unique potential for the construction of various architectures. In the past decades, many carbon allotropes such as carbon fullerenes,[1] nanotubes,[2] and graphene[3] have been synthesized and characterized. Over thirty years ago, Baughman and Eckhardt predicted two-dimensional (2D) sheets of carbon, called graphyne (GY), including α-, β-, and γ-GY.[4] Among them, γ-GY exhibits high stability and semiconductor features.[5] With the increase of acetylenic linkages among adjacent aromatic rings, more members of the GY family, such as graphdiyne (GDY), graph-3-yne, graph-4-yne and graph-5-yne, were obtained.[6] γ-GY consisting of sp and sp^2 carbon atoms can be viewed as resulting from the substitution of the carbon–carbon bonds in graphene by acetylenic (–C≡C–) linkages. The acetylenic linkage is an efficient connecting unit because of the structural linearity without any existing fluctuation arising from cis–trans isomerization.[7] Therefore, the introduced acetylenic linkages create a planar network of γ-GY with high surface area and porosity, making its structural, mechanical, thermal, optical and particularly electrical properties quite different from those of graphene or carbon nanotubes.[8–11] For example, the acetylenic linkages in γ-GY and GDY endow them with significant band gaps (0.47 and 0.52 eV, respectively).[6] This is different from graphene, of which the intrinsic zero band gap significantly limits its practical applications in electronic devices and thus considerable efforts such as increasing the thickness,[12,13] introducing a substrate[14], chemical doping[15] and strain engineering[16] have been made to open the band gap in graphene.

Experimentally, large area GDY was synthesized on the surface of copper *via* a cross-coupling reaction, showing excellent semiconducting properties.[7] Subsequently, GDY nanotube arrays were also synthesized through an anodic aluminum oxide (AAO) template catalyzed with copper foil.[17] The breakthrough in the synthesis of GDY has stimulated great interest in studying new members of the GY family (*i.e.*, γ-GY and graph-4-yne)[18,19] for promising applications such as hydrogen storage[20,21] and lithium-ion batteries (LIBs).[22,23] For instance, it's reported that the maximum capacity of graph-4-yne for Li storage could reach as high as 947 mA h g^{-1}.[19] It should be noted here that most theoretical studies focus on monolayer materials for use in LIB anodes, which may provide a limited view of the performance as the interlayer chemical interaction of these materials in reality is neglected. The interlayer chemical

[a]Department of Engineering Mechanics, School of Civil Engineering, Wuhan University, Wuhan, Hubei 430072, China. E-mail: enlaigao@whu.edu.cn; ze.liu@whu.edu.cn

[b]Beijing Key Laboratory of Ionic Liquids Clean Process, CAS Key Laboratory of Green Process and Engineering, Institute of Process Engineering, Chinese Academy of Sciences, Beijing 100190, China

interaction of these materials remains challenging for use in LIB anode materials and thus their effect on the performance needs to be quantitatively evaluated.

In this work, we report a new member of GY with an ultra-high specific surface area of 4255 m^2 g^{-1} and direct band gap of 1.00 eV (HSE06), called C_{68}-GY. Its stability is carefully checked by both phonon dispersion calculations and *ab initio* molecular dynamics (AIMD). The smaller in-plane tensile stiffness ($\sim$50.5 N m^{-1}) and out-of-plane bending stiffness ($\sim$0.5 eV) than those of graphene (in-plane tensile stiffness 350 N m^{-1} and out-of-plane bending stiffness 1.4 eV) indicate the exceptional flexibility of C_{68}-GY. The calculated highly efficient charge transfer from adsorbed Li ions to C_{68}-GY, low diffusion barrier of Li ions in C_{68}-GY for fast charge/discharge rates, and ultra-high specific capacity (monolayer: 1954 mA h g^{-1}, bilayer: 1675 mA h g^{-1}) make C_{68}-GY an ideal candidate for anode materials of LIBs.

2. Computational methods

First principles calculations are carried out in the framework of density functional theory as implemented in the Vienna *ab initio* simulation package (VASP).[24,25] The projector augmented wave method is used to treat the interactions between electrons and ions.[26] General gradient approximation is employed with the Perdew–Burke–Ernzerhof (PBE) functional to describe the exchange and correlation interactions between electrons unless noted ortherwise.[27] The energy cutoff is set to 600 eV for all calculations. The *K*-point density used in the calculations is >50 Å based on the Monkhorst–Pack scheme[28]. The cell parameters and ionic positions are fully optimized until the force on each atom is converged below 0.01 eV $Å^{-1}$. In order to avoid inter-actions between periodic images, a vacuum separation of 30 Å is adopted. The electronic properties are calculated by both using PBE and hybrid functionals (HSE06).[29] Density functional perturbation theory[30] calculations are performed to obtain the phonon dispersion combining VASP and the open source code Phonopy.[31]

3. Results and discussion

3.1. Structure and chemical analysis

Similar to γ-GY (Fig. S1†), the new form of GY consists of acetylenic linkages and aromatic rings as shown in Fig. 1a. The primitive cell contains 24 carbon atoms (Fig. 1b). The optimized lattice constant (10.84 Å) is larger than that of γ-GY (6.86–6.89 Å), but C_{68}-GY has the same hexagonal symmetry ($P6/mmm$: D_{6h}) as γ-GY.[4-6] From Fig. 1a, it can be observed that two acetylenic linkages concurrently join to the neighboring aromatic rings resulting in an octatomic ring. Besides, the angles between acetylenic linkages and aromatic rings are obtuse ($\alpha_1 = 125.8°$), differing from those in GY (60°). According to the previous naming convention of GY,[32] this new GY is named C_{68}-GY. As we know, there are three types of C–C bonds in γ-GY (Fig. S1b†): sp^2–sp^2 ($B_1 = 1.436$ Å), sp^2–sp ($B_2 = 1.408$ Å) and sp–sp ($B_3 = 1.223$ Å),[5] while there are four types of C–C bonds in C_{68}-GY (Fig. 1b): including two types of sp^2–sp^2 ($B_1 = 1.462$ Å and $B_2 = 1.397$ Å), sp^2–sp ($B_3 = 1.413$ Å) and sp–sp ($B_4 = 1.227$ Å). For further insights into the bond characteristics, total electron densities of C_{68}-GY are plotted (Fig. 1c). The electron densities of sp–sp bonds (B_4) are obviously higher than those of others, suggesting stronger electron delocalization in the sp–sp bonds (Fig. 1d). The angles between sp^2–sp bond (B_3) and sp–sp bond (B_4) in the acetylenic linkages of C_{68}-GY are of obtuse angle ($\alpha_2 = 155.8°$), which is attributed to the electrostatic repulsive interactions between two adjacent acetylenic linkages in the same octatomic ring. Meanwhile, the interactions further stretch the shared bonds (B_1) between octatomic and aromatic
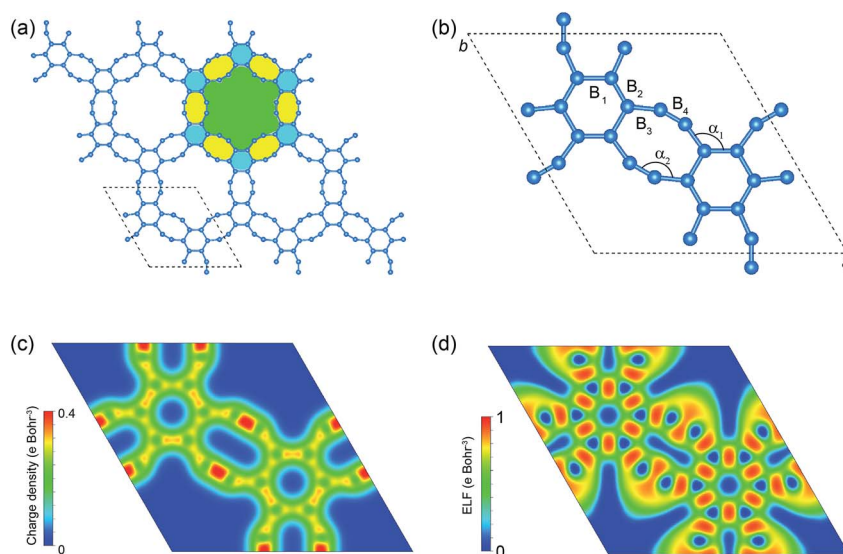

Fig. 1 (a) Schematic diagram of C_{68}-GY, and (b) its primitive cell. Color coding is yellow for octatomic rings, cerulean for aromatic rings, and green for the pores. B_1, B_2, B_3 and B_4 denote the different bonds, and α_1 and α_2 are two angles. The plotted iso-surfaces of (c) total electron density and (d) electron location function (ELF) are shown in the primitive cell.

rings, thus resulting in the bond B_1 longer than B_2, which accounts for two types of sp^2–sp^2 bonds in aromatic rings. Meanwhile, the octatomic and aromatic rings together form a pore with a diameter of 8.22 Å (Fig. 1a), much larger than those in graph-n-yne ($n = 1, 2, 3, 4$ and 5).[33] In particular, the theoretical specific surface area is 4255 m^2 g^{-1}, larger than those of activated carbon ($\sim$2000 m^2 g^{-1})[34] and graphene (experimental data: $\sim$1500 m^2 g^{-1}, theoretical calculation: $\sim$2620 m^2 g^{-1}),[35] indicating its potential application for gas adsorption and purification. Besides, two methods are used to determine the van der Waals (vdW) thickness of monolayer C_{68}-GY by characterizing the weak interlayer interactions of C_{68}-GY. The first one is to calculate the energy curve for two separated C_{68}-GY *versus* the different distances (Fig. 2a), from which we find that the equilibrium distance of d_{vdW} is 3.76 Å with an adhesion energy of 104.3 mJ m^{-2}. The other method is to fully optimize the C_{68}-GY bilayer with an initial separation of 4 Å. The optimized energy of bilayer C_{68}-GY is compared with that of

monolayer C_{68}-GY to obtain an adhesion energy of 106.6 mJ m^{-2}. The smaller adhesion energy of 104.3–106.6 mJ m^{-2} found here than that of γ-GY (223.5 mJ m^{-2})[9] is attributed to the sparser distribution of in-plane carbon atoms.

3.2. Stability

First, the thermal stability of C_{68}-GY with respect to its cohesive energy is evaluated. According to eqn (1), the cohesive energy is determined to be 7.09 eV per atom.

$$E_{coh} = \frac{24E_C - E_{C_{68}\text{-GY}}}{24} \tag{1}$$

where E_C and $E_{C_{68}\text{-GY}}$ denote the energy of the isolated carbon atom and C_{68}-GY. Compared with GY and graphene (Fig. 2b), the stability of C_{68}-GY closely follows that of γ-GY (7.21 eV)[5] and graphene (8.11 eV).[36] Afterwards, the dynamic stability of C_{68}-GY is verified by phonon dispersion calculation, where the absence of imaginary modes[37] indicates the dynamic stability of the C_{68}-
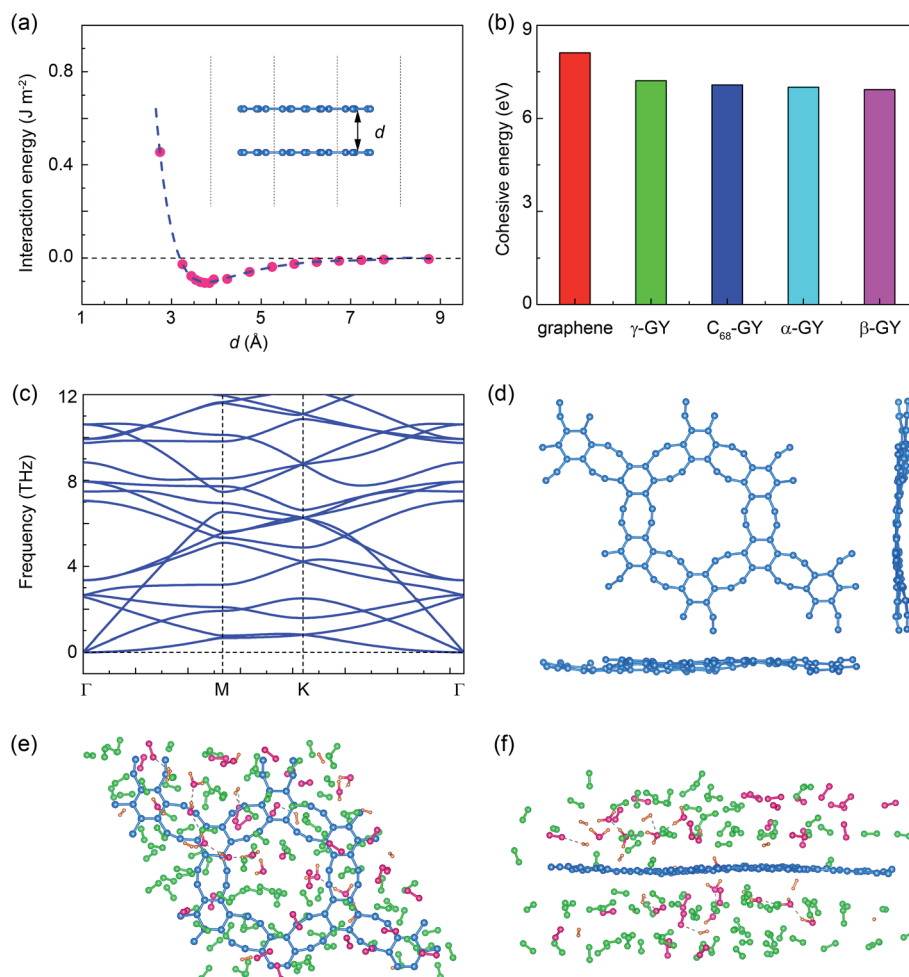
Fig. 2 (a) The interaction energy as a function of various separation d values, between two layers of C_{68}-GY (inset). The blue dashed line denotes the fitting curve for the red points. (b) The comparison of cohesive energies of graphene, α-, β-, and γ-GY with C_{68}-GY. The data for graphene, α-GY, β-GY and γ-GY are obtained from ref. 5 and 36. (c) The calculated phonon dispersion spectrum of C_{68}-GY. (d) The snapshots (top and side views) taken from AIMD simulations of C_{68}-GY. (e and f) The snapshots (top and side views) taken from AIMD simulations of C_{68}-GY in the atmosphere, where the ratio of the molecular numbers is set to be $N_2 : O_2 : H_2O : H_2 = 22 : 6 : 3 : 3$ and the blue, red, green and orange spheres represent C, O, N and H atoms, respectively.

GY monolayer (Fig. 2c). Meanwhile, the thermodynamic stability in a supercell ($2 \times 2 \times 1$) is evaluated by performing AIMD simulations at 300 K for 10 ps. The temperature is controlled by using the Nosé–Hoover thermostat. During the AIMD simulation, C_{68}-GY upholds its structural integrity with only slight corrugation because of thermal fluctuations (Fig. 2d). Subsequently, we probe the chemical stability of C_{68}-GY under ambient conditions with common molecules in the atmosphere (the molecular ratio is set as $N_2 : O_2 : H_2O : H_2 = 22 : 6 : 3 : 3$) for 10 ps in the NPT ensemble with a controlled temperature of 300 K and pressure of 0 bar. A slight fluctuation of lattice constants (Fig. S2a†) and no bonds formed or broken during the whole AIMD simulations (Fig. 2e–f) suggest the great chemical stability of C_{68}-GY under ambient conditions. The above results confirm the remarkable energetic, dynamic, thermodynamic and chemical stabilities of C_{68}-GY. In addition, recently GDY and graph-4-yne have been successfully synthesized on the surface of copper foil,[7,19] and thus C_{68}-GY could be expected to be grown on the copper substrate.

3.3. Mechanical properties

To investigate the mechanical properties of C_{68}-GY, tensile tests for monolayer C_{68}-GY in a rectangle cell are performed (Fig. 3a,b). The uniaxial stress–strain in Fig. 3c shows that the tensile strength (σ) along x- and y-directions is 21.7 N m^{-1} (58.0 GPa, using a thickness of 3.74 Å for monolayer C_{68}-GY) and 14.7 N m^{-1} (39.3 GPa), corresponding to the failure strain of 32% and 20%, respectively. The larger failure strain along the x-direction is attributed to some acetylenic linkages directly bearing the tensile load. Similar to graphene,[38,39] C_{68}-GY has an almost isotropic in-plane elastic response with an in-plane tensile stiffness of ~50.5 N m^{-1} (135.0 GPa), which is smaller than those of graphene (350 N m^{-1} and 1050 GPa).[39] Note that, as $\varepsilon_x = 25\%$, the stress–strain and strain energy–strain

responses abruptly change, implying that the atomic structure of C_{68}-GY has a significant transformation. As shown in Fig. 3b, we find that only the acetylenic linkages directly bear load along the x-direction, and other acetylenic linkages are broken and then reconstructed. In addition to in-plane mechanical behaviors, we also examine its out-of-plane elasticity, $i.e.$ bending stiffness D. Two methods can be used to calculate D. The first one is to fit the bending energy per unit area E_{ben} of a C_{68}-GY nanotube as a function of its radius R, based on the equation $E_{ben} = DR^{-2}/2$;[40] The second one is to fit the phonon dispersions $\omega(q)$ with the equation $\omega^2 = (D/\rho)q^4$ according to the quadratic dispersion of the flexural phonon mode ZA,[41] where ρ is the areal density of C_{68}-GY (4.70×10^{-7} kg m^{-2}). Due to the first method requiring high computational costs, the second approach is adopted in this work (Fig. S2b†). The calculated D values along Γ–M and Γ–K are both ~0.50 eV. In the same way, a D value of 1.43 eV for graphene is calculated (Fig. S2c†), coinciding with previous DFT calculations (1.44 eV).[42] Moreover, the comparison of mechanical properties with those of other typical carbon allotropes is provided in Table S1.† The small in-plane tensile stiffness and out-of-plane bending stiffness make C_{68}-GY an atomic membrane with exceptional flexibility.

3.4. Electronic properties

The band structure and projected density of states (PDOS) are computed with the PBE functional. Unlike γ-GY (at the M point),[43] the conduction band minimum (CBM) and valence band maximum (VBM) of C_{68}-GY are located at the K point in the Brillouin zone. The band gap of 0.51 eV (Fig. 4a) is larger than that of γ-GY (0.46 eV).[5] From the PDOS (Fig. S3a†), only contribution of p_z orbitals is found around the Fermi level (−1.3 eV to 2.6 eV). Therefore, only bands corresponding to π and π* states are present in this gap. Because the PBE functional tends to underestimate the band gaps of materials,[44]
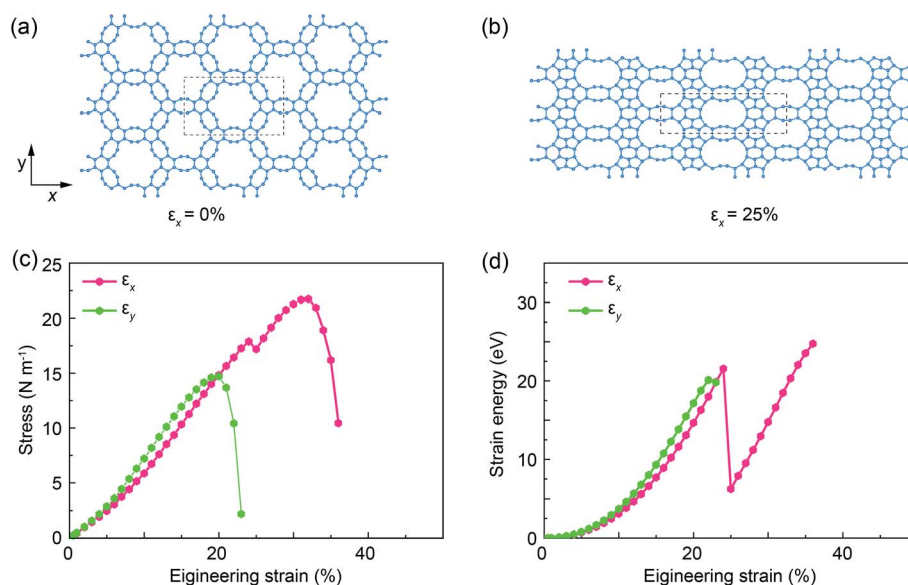

Fig. 3 (a) The schematic diagram of uniaxial tensile tests using a rectangular cell (dashed line); (b) the atomic configuration under a uniaxial tension of $\varepsilon_x = 25\%$; (c) the stress and (d) strain energy responses under the uniaxial tension.
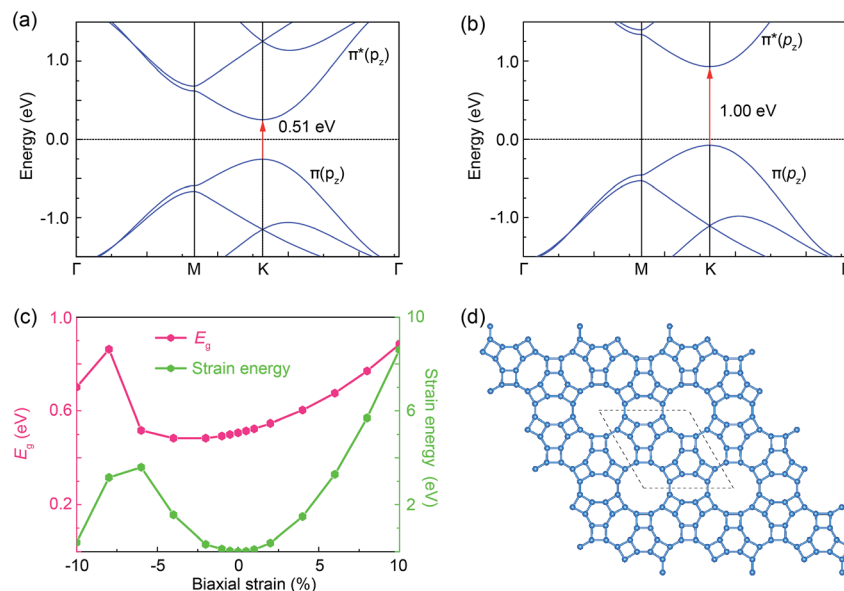
Fig. 4 Band structures of the C_{68}-GY monolayer are calculated by using (a) PBE and (b) HSE06 functionals following the path $\Gamma-M-K-\Gamma$ of the first Brillouin zone. (c) The calculated band gap E_g and strain energy under different biaxial strains. (d) The atomic configuration of C_{68}-GY at a biaxial strain of -8%.

a more reliable method with the HSE06 functional is used to recompute the band structure ($E_g = 1.00$ eV) as depicted in Fig. 4b. Furthermore, we calculate the effective masses utilizing the expression:

$$m^* = \frac{\hbar^2}{\partial^2 E / \partial k^2} \quad (2)$$

The $|m^*|$ values along the K–M direction are larger than those along the K–Γ direction. Meanwhile, biaxial strain (ε) ranging from -10% to 10% is used to tune the electronic properties of C_{68}-GY. The band gap E_g, strain energy, and the effective masses for electrons and holes are calculated corresponding to the strain (Fig. 4c and Table S2†). The E_g and $|m^*|$ both increase with the increase of strain. As $\varepsilon = 10\%$, E_g increases to be 0.88 eV. During the compression, E_g first decreases and then increases, whereas the band structures show an indirect feature as C_{68}-GY is further compressed to an ε of about -8% (Fig. S4†). Meanwhile, the strain energies abnormally decrease at an ε of about -8%, implying that the structures substantially change. We checked the structures corresponding to this critical strain and confirmed that a phase transition occurs, in which the original octatomic rings reconstruct to be tetratomic and new octatomic rings (Fig. 4d). Finally, the carrier mobilities of C_{68}-GY are given by[45]

$$\mu_{2D} = \frac{e\hbar^3 C_{2D}}{k_B T |m^*| m_d (E_1)^2} \quad (3)$$

where m_d is the average effective mass determined by $\sqrt{m_x^* m_y^*}$, m_x^* and m_y^* are the effective mass (m^*) along the x- and y-directions of transport, respectively, C_{2D} is the elastic constant and E_1 is the DP constant (Fig. S5†). C_{2D} can be determined by

the calculations of the elastic constant matrix of monolayer C_{68}-GY. Hence, the carrier mobilities along x- and y-directions are obtained (Table 1). For monolayer C_{68}-GY at room temperature (300 K), the carrier mobility is as high as 1.81×10^5 to 2.97×10^5 cm^2 V^{-1} s^{-1}, which is much higher compared to those of other 2D materials such as MoS$_2$ (ref. 46) and black phosphorene.[45] The high carrier mobility mainly originates from the small deformation potential (0.4 eV) that is much smaller than those of graphene (5.0 eV),[47] MoS$_2$ (3.9 eV)[46] and phosphorene (2.7 eV).[45] The tunable electronic structure and excellent electronic conductance make C_{68}-GY a promising candidate for future flexural electronic devices.

3.5. The application of C_{68}-GY as the anode material for lithium-ion batteries

The promising application of C_{68}-GY as the anode material for LIBs is investigated in this part. First, the strongest adsorption site for an isolated Li on the C_{68}-GY monolayer ($2 \times 2 \times 1$) is determined by evaluating the adsorption energy E_{ad}:

$$E_{ad} = \frac{E(m@C_{68}\text{-GY}) - E(C_{68}\text{-GY}) - m\mu(\text{Li})}{m} \quad (4)$$

where $E(C_{68}$-GY) and $E(m@C_{68}$-GY) are the total energies of C_{68}-GY before and after adsorption of m Li ions, respectively, and $\mu(\text{Li})$ is the chemical potential of Li.[48] Five intercalation positions denoted as S1–S5 are considered (Fig. 5a). The DFT-D3 method of Grimme is employed for the corrections of the van der Waals interactions.[49] The results show that the most favorite site of Li adsorbed on C_{68}-GY is S4 with the lowest E_{ad} of -3.01 eV (Table 2). The absolute values of adsorption energies are all larger than those of graphite (-0.78 eV),[50] suggesting a strong ionic binding between Li ions and the C_{68}-GY substrate. The charge density difference is plotted as depicted

Table 1 The calculated carrier mobility μ_{2D} at 300 K for monolayer C_{68}-GY along the x- and y-directions, including the in-plane elastic constants C_{2D}, DP constant, E_1 and effective mass m^*

Carrier type	m_x^*/m_0	m_y^*/m_0	E_{1x} (eV)	E_{1y} (eV)	C_{2D_x} (N m^{-1})	C_{2D_y} (N m^{-1})	μ_{2D_x} (10^5 cm^2 V^{-1} s^{-1})	μ_{2D_y} (10^5 cm^2 V^{-1} s^{-1})
Electron	0.214	0.185	0.382	0.406	78.202	78.202	2.681	2.745
Hole	−0.223	−0.193	−0.446	−0.374	78.202	78.202	1.810	2.974

in Fig. 5c–e, showing that Li is ionized as adsorbed on the surface of C_{68}-GY. This observation coincides with the Bader charge analysis revealing that Li transfers charges of 0.91e (S1), 0.98e (S3) and 0.92e (S4) to C_{68}-GY, respectively, approaching that of MoN$_2$ (0.89e).[51] These results clearly demonstrate that the Li ion is in the cationic state and is chemically adsorbed on the C_{68}-GY monolayer. Moreover, PDOS calculations (Fig. S3b–d†) clearly show the metallic characters of C_{68}-GY that adsorbed one Li, arising from p$_z$ orbitals around the Fermi level to the

left. The excellent electrical conduction is of significance for anode materials.

Besides, the charge/discharge rate is of great importance for the performance of anode materials, which depends upon the mobility of ions. Therefore, we probe the diffusion behaviors of Li ions over and through C_{68}-GY using the climbing-image nudged elastic band (CI-NEB) method.[52] For the in-plane diffusion, the diffusion paths P1, P2, P3 and P4 are considered (Fig. 5b). Among them, P1 and P2 are the paths through
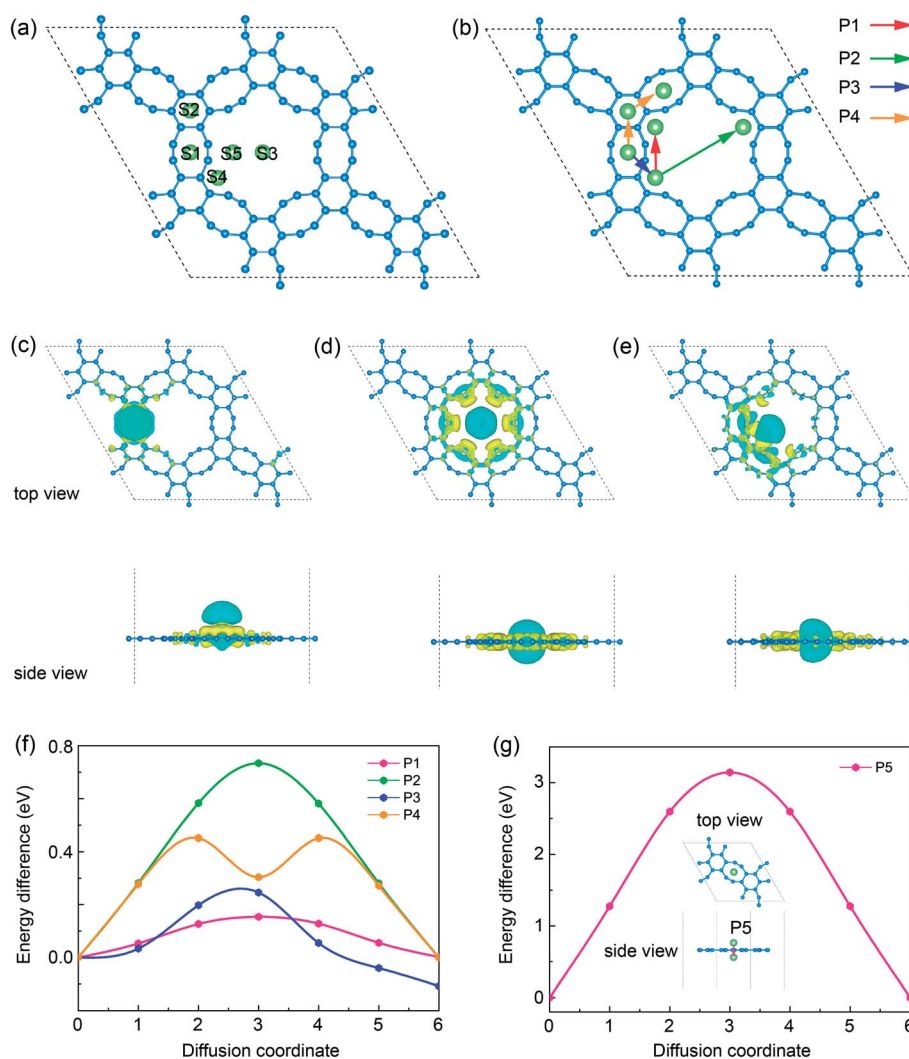
Fig. 5 (a) Five potential different adsorption sites of an intercalated Li ion in the C_{68}-GY monolayer, and the blue and green spheres represent C and Li atoms, respectively. (b) Schematics of the diffusion P1 to P4 (top view). Top and side views of the differential charge density of one Li ion adsorbed on (c) S1, (d) S3 and (e) S4 with an isosurface value of 0.0006 e Bohr^{-3}. Color coding is yellow for charge gain and green for charge loss. The diffusion barrier profiles of (f) in-plane diffusion (P1–P4) and (g) the out-plane diffusion (P5).

Table 2 The adsorption energy (E_{ad}) and height (h) for the five different adsorption sites in the supercell ($2 \times 2 \times 1$) of monolayer C_{68}-GY

Monolayer	Sites	E_{ad} (eV)	h (Å)[a]
$2 \times 2 \times 1$	S1	−2.90	1.67
	S2	−2.62	1.77
	S3	−2.28	0
	S4	−3.01	0.12
	S5	−2.86	0

[a] The adsorption height h denotes the vertical distance between Li ions and the C_{68}-GY monolayer.

which Li migrates from the most favorite site (S4) to another one. For the out-of-plane diffusion paths, P5 denotes the path passing through S1 (octatomic ring) from one side to another. The diffusion barriers of ions over and through monolayer C_{68}-GY are shown in Fig. 5f–g, involving the low diffusion barriers of 0.13 eV, 0.25 eV and 0.45 eV for P1, P3 and P4, respectively. For the out-of-plane diffusion, P5 uncovers the highest diffusion barrier of 3.14 eV. It can be understood that the small pore size of the octatomic ring results in a larger repulsive Coulomb interaction, which significantly enhances the diffusion barrier. These diffusion barriers of in-plane diffusion are smaller than those of the well-studied electrode materials, such as bulk silicon (0.57 eV)[53,54] and TiO_2-based polymorphs (0.65 eV).[55,56] To further probe the effect of interlayer chemical interaction on the diffusion properties, we calculate the diffusion path P1 (Fig. 5b) for bilayer C_{68}-GY (Fig. S6a†) with a barrier of 8.4 meV. From the barrier profile, the state at coordinate 3 is more stable than the initial/final state (Li on S4). Conversely, it can be speculated that the barrier of Li diffusing from coordinate 3 to the transition state (TS) is 57 meV (Fig. S6b†). Compared to the diffusion barriers of Li on the monolayer, the weak interlayer vdW interaction reduces the diffusion barriers and alters the most favorite site where Li is intercalated in C_{68}-GY.

Furthermore, we evaluated the Li concentration intercalated in C_{68}-GY to determine the specific capacity for Li storage. The specific capacity is calculated by:

$$C = \frac{xF}{M} \tag{5}$$

where x is the concentration of Li ions in C_{68}-GY (the ratio between intercalated Li ions and carbon atoms in the hybrid system), F denotes the Faraday constant 26.8 A h mol^{-1}, and M is the mass of carbon atoms. To explore the stabilities of the intermediate product (Li_xC) with various Li ion concentrations (x), the formation energy is calculated to plot the convex hull. There are two methods used to calculate the formation energy.[57–59] The first one is to use metallic Li and non-lithiated C_{68}-GY as reference states; the second one is to use non-lithiated C_{68}-GY and the fully lithiated C_{68}-GY as reference states. Herein the second method is adopted, and the formation energy of Li_xC is calculated by:

$$E_{form} = E - x \times E_{LiC} - (1 - x) \times E_C \tag{6}$$

where E is the total energy of the configuration per $Li_x\varnothing_{1-x}C$ formula unit ($0 < x < 1$), E_{LiC} is the energy of LiC, and E_C is the energy of C_{68}-GY per carbon atom. Fig. 6a displays the formation energies for Li_xC with varying Li concentrations for monolayer C_{68}-GY. AIMD simulations for the configurations of LiC are performed under the NPT ensemble with a temperature of 300 K and pressure of 0 bar to investigate the thermodynamic stability (Fig. S7a†). After running for 10 ps, LiC still holds the structural integrity but with corrugations leading to lattice contraction within the range of −5% (Fig. S7b†) accompanied by some of the original octatomic rings being reconstructed to be tetratomic and new octatomic rings, indicating a phase transition (Fig. S7c and d†). Besides, the volume expansion or contraction is considered during the adsorption process which is a key parameter controlling whether electrode reactions are reversible. As we know, the volume of 2D materials is not easy to identify. Instead, the in-plane expansion or contraction is considered using the lattice constant (a) ratio, which can be calculated using a/a_0, where a_0 and a are the lattice constants of C_{68}-GY before and after adsorption of Li ions, respectively. Along these structures with the minimum formation energy (Fig. 6a, green points) as depicted in Fig. S8,† the adsorption energy and lattice changes are calculated as shown in Fig. S9a.† The negative adsorption energies demonstrate that these adsorption processes are exoergic without formation of Li clusters. Tiny lattice changes of C_{68}-GY manifest that the intercalation of Li ions weakly influences the in-plane
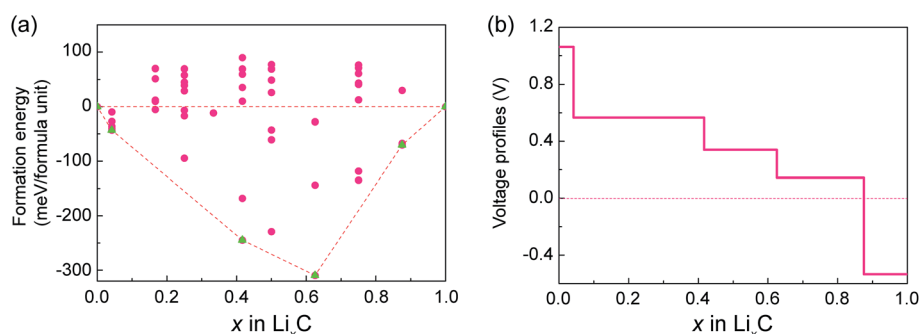
Fig. 6 (a) Formation energies calculated for different configurations of C_{68}-GY intercalated Li ions; (b) the calculated voltage profile along the minimum energy path of formation energies, green points of (a).

expansion or contraction. On the one hand, with the increase of Li ions intercalated in C_{68}-GY, the repulsive electrostatic interactions between Li ions will induce in-plane lattice expansion (Fig. S8a and b†). On the other hand, C_{68}-GY with weak out-of-plane resistance is apt to be corrugated if Li more ions asymmetrically distribute on C_{68}-GY (Fig. S8c and d†), which thus results in the in-plane contraction of the system. These two competitive mechanisms explain the trend of lattice constant changes. For Li intercalated in bilayer C_{68}-GY, three configurations with varying Li concentrations (Fig. S8e–g†) are probed with negative adsorption energies (Table 3). Meanwhile, the calculated formation energies further show that the intermediate configurations with Li ions intercalated in bilayer C_{68}-GY are also stable.

Afterwards, the OCV profiles are calculated, which is a measurement of the performance of the anode materials of LIBs. The charge/discharge processes of C_{68}-GY follow the half-cell reaction vs. Li/Li$^+$:
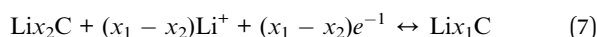
$$\text{Li}x_2\text{C} + (x_1 - x_2)\text{Li}^+ + (x_1 - x_2)e^{-1} \leftrightarrow \text{Li}x_1\text{C} \qquad (7)$$

where $x_1 > x_2$. Then the voltage is

$$V = -\frac{G(\text{Li}x_1\text{C}) - G(\text{Li}x_2\text{C}) - (x_1 - x_2)G(\text{Li})}{(x_1 - x_2)ze} \qquad (8)$$

where G is the Gibbs free energy of the compound, $\Delta x = x_1 - x_2$ ($x_1 > x_2$) and z represents the charge of the metal ion (here $z = 1$ for Li). Since the contribution of entropy ($T\Delta S \approx 25$ meV at 300 K) and enthalpy ($P\Delta V$ in the order of 1.0^{-5} eV) can be neglected,[60] the Gibbs free energy ($\Delta G = \Delta E + P\Delta V - T\Delta S$) can be approximated as the internal energy ΔE.[61] Within this approximation, the voltage profiles are calculated along these structures with minimum formation energy (Fig. 6a).[62] From the voltage profile (Fig. 6b), as x increases to 0.875, corresponding to a specific capacity of 1954 mA h g^{-1}, the voltage decreases to 0.14 V. As x approaches 1.0, the voltage would decrease to −0.54 V, indicating that the lithiation process will stop. Similarly, for Li intercalations in bilayer C_{68}-GY, the calculated voltage is 0.37 V when x increases to 0.75, corresponding to a capacity of 1675 mA h g^{-1}. As x increases to 1.125, the voltage of $\text{Li}_{1.125}\text{C}$ decreases to −0.11 V. Besides, the comparisons of the specific capacities of C_{68}-GY with other typical carbon allotropes are shown in Fig. S9b,† indicating that C_{68}-GY is an ideal candidate for anode materials of LIBs with high specific capacity.

Table 3 The adsorption energy E_{ad}, formation energy E_{form}, and the lattice constant ratios, a/a_0 for Li ions in bilayer C_{68}-GY. The formation energy for these bilayer configurations is calculated by using non-lithiated C_{68}-GY and the lithiated $\text{Li}_{1.125}\text{C}$ as reference states

Bilayer	$\text{Li}_{0.375}\text{C}$	$\text{Li}_{0.75}\text{C}$	$\text{Li}_{1.125}\text{C}$
E_{ad} (eV)	−0.44	−0.55	−0.43
E_{form} (meV per formula unit)	−3.6	−91.8	0
a/a_0	0.998	0.991	1.032

4. Conclusion

In this work, we predict a novel allotropy of GY using first principles calculations, named C_{68}-GY. The remarkable energetic, dynamic, thermodynamic and chemical stabilities of C_{68}-GY are confirmed by the first principles calculations. The unique atomic structures endow it with ultrahigh specific surface area (4255 m^2 g^{-1}), high ductility (20–32%) and excellent elastic flexibility (in-plane tensile stiffness ~50.5 N m^{-1} and out-of-plane bending stiffness ~0.5 eV). The calculated electronic structure shows a direct gap in the band structure (0.51 eV and 1.00 eV at PBE and HSE06 levels, respectively). The tunability of the band structure by strain-engineering is further explored. The band gap is observed to be increasing with increasing strain. The calculated high carrier mobilities of 1.81×10^5 to 2.97×10^5 cm^2 V^{-1} s^{-1} indicate the potential applications of C_{68}-GY in electronic devices. Finally, C_{68}-GY possesses a low diffusion energy barrier for fast charge/discharge rates as well as high specific capacities (monolayer: 1954 mA h g^{-1}, bilayer: 1675 mA h g^{-1}). These exceptional electrical conductivity, fast charge/discharge rates and high capacity suggest that C_{68}-GY can be utilized as a promising anode material for LIBs with high performance.

Conflicts of interest

There are no conflicts to declare.

Acknowledgements

References

1 H. W. Kroto, J. R. Heath, S. C. O'Brien, R. F. Curl and R. E. Smalley, *Nature*, 1985, **318**, 162–163.

2 S. Iijima, *Nature*, 1991, **354**, 56–58.

3 K. S. Novoselov, A. K. Geim, S. V. Morozov, D. Jiang, Y. Zhang, S. V. Dubonos, I. V. Grigorieva and A. A. Firsov, *Science*, 2004, **306**, 666–669.

4 R. Baughman, H. Eckhardt and M. Kertesz, *J. Chem. Phys.*, 1987, **87**, 6687–6699.

5 A. R. Puigdollers, G. Alonso and P. J. C. Gamallo, *Carbon*, 2016, **96**, 879–887.

6 N. Narita, S. Nagai, S. Suzuki and K. Nakao, *Phys. Rev. B: Condens. Matter Mater. Phys.*, 1998, **58**, 11009–11014.

7 G. Li, Y. Li, H. Liu, Y. Guo, Y. Li and D. Zhu, *Chem. Commun.*, 2010, **46**, 3256–3258.

8 Y. Zhang, Q. Pei and C. Wang, *Appl. Phys. Lett.*, 2012, **101**, 081909.

9 S. W. Cranford and M. J. Buehler, *Carbon*, 2011, **49**, 4111–4121.

10 J. Kang, J. Li, F. Wu, S.-S. Li and J.-B. Xia, *J. Phys. Chem. C*, 2011, **115**, 20466–20470.

11 T. Ouyang, Y. Chen, L.-M. Liu, Y. Xie, X. Wei and J. Zhong, *Phys. Rev. B: Condens. Matter Mater. Phys.*, 2012, **85**, 235436.

12 Y. Zhang, T.-T. Tang, C. Girit, Z. Hao, M. C. Martin, A. Zettl, M. F. Crommie, Y. R. Shen and F. J. N. Wang, *Nature*, 2009, **459**, 820–823.

13 E. V. Castro, K. Novoselov, S. Morozov, N. Peres, J. L. Dos Santos, J. Nilsson, F. Guinea, A. Geim and A. C. J. P. r. l. Neto, *Phys. Rev. Lett.*, 2007, **99**, 216802.

14 S. Y. Zhou, G. H. Gweon, A. V. Fedorov, P. N. First, W. A. de Heer, D. H. Lee, F. Guinea, A. H. Castro Neto and A. Lanzara, *Nat. Mater.*, 2007, **6**, 770–775.

15 W. Zhang, C.-T. Lin, K.-K. Liu, T. Tite, C.-Y. Su, C.-H. Chang, Y.-H. Lee, C.-W. Chu, K.-H. Wei, J.-L. Kuo and L.-J. Li, *ACS Nano*, 2011, **5**, 7517–7524.

16 G. Gui, J. Li and J. J. P. R. B. Zhong, *Phys. Rev. B: Condens. Matter Mater. Phys.*, 2008, **78**, 075435.

17 G. Li, Y. Li, X. Qian, H. Liu, H. Lin, N. Chen and Y. Li, *J. Phys. Chem. C*, 2011, **115**, 2611–2615.

18 Q. Li, Y. Li, Y. Chen, L. Wu, C. Yang and X. Cui, *Carbon*, 2018, **136**, 248–254.

19 J. Gao, J. Li, Y. Chen, Z. Zuo, Y. Li, H. Liu and Y. Li, *Nano Energy*, 2018, **43**, 192–199.

20 S. Kumar and Dhilip Kumar Thogluva Janardhanan, *ACS Appl. Mater. Interfaces*, 2017, **9**, 28659–28666.

21 H. J. Hwang, Y. Kwon and H. Lee, *J. Phys. Chem. C*, 2012, **116**, 20220–20224.

22 H. Zhang, M. Zhao, X. He, Z. Wang, X. Zhang and X. Liu, *J. Phys. Chem. C*, 2011, **115**, 8845–8850.

23 H. J. Hwang, J. Koo, M. Park, N. Park, Y. Kwon and H. Lee, *J. Phys. Chem. C*, 2013, **117**, 6919–6923.

24 G. Kresse and J. Hafner, *Phys. Rev. B: Condens. Matter Mater. Phys.*, 1994, **49**, 14251–14269.

25 G. Kresse and J. Furthmüller, *Phys. Rev. B: Condens. Matter Mater. Phys.*, 1996, **54**, 11169–11186.

26 P. E. Blöchl, *Phys. Rev. B: Condens. Matter Mater. Phys.*, 1994, **50**, 17953–17979.

27 J. P. Perdew, K. Burke and M. Ernzerhof, *Phys. Rev. Lett.*, 1996, **77**, 3865–3868.

28 H. J. Monkhorst and J. D. Pack, *Phys. Rev. B: Solid State*, 1976, **13**, 5188–5192.

29 J. Heyd, G. E. Scuseria and M. Ernzerhof, *J. Chem. Phys.*, 2003, **118**, 8207–8215.

30 S. Baroni, S. De Gironcoli, A. Dal Corso and P. Giannozzi, *Rev. Mod. Phys.*, 2001, **73**, 515–562.

31 A. Togo and I. Tanaka, *Scr. Mater.*, 2015, **108**, 1–5.

32 H. Lu and S.-D. Li, *J. Phys. Chem. C*, 2013, **1**, 3677–3680.

33 S. Lin and M. J. Buehler, *Nanoscale*, 2013, **5**, 11801–11807.

34 S. Y. Lu, M. Jin, Y. Zhang, Y. B. Niu, J. C. Gao and C. M. Li, *Adv. Energy Mater.*, 2018, **8**, 1702545.

35 Z.-S. Wu, G. Zhou, L.-C. Yin, W. Ren, F. Li and H.-M. Cheng, *Nano Energy*, 2012, **1**, 107–131.

36 V. O. Özçelik and S. Ciraci, *J. Phys. Chem. C*, 2013, **117**, 2175–2182.

37 Y. Li, Y. Liao and Z. Chen, *Angew. Chem., Int. Ed.*, 2014, **53**, 7248–7252.

38 X. Wei, B. Fragneaud, C. A. Marianetti and J. W. Kysar, *Phys. Rev. B: Condens. Matter Mater. Phys.*, 2009, **80**, 205407.

39 F. Liu, P. Ming and J. Li, *Phys. Rev. B: Condens. Matter Mater. Phys.*, 2007, **76**, 064120.

40 Z. Zhang, Y. Yang, E. S. Penev and B. I. Yakobson, *Adv. Funct. Mater.*, 2017, **27**, 1605059.

41 L. J. Karssemeijer and A. Fasolino, *Surf. Sci.*, 2011, **605**, 1611–1615.

42 Y. Wei, B. Wang, J. Wu, R. Yang and M. L. Dunn, *Nano Lett.*, 2013, **13**, 26–30.

43 K. Srinivasu and S. K. Ghosh, *J. Phys. Chem. C*, 2012, **116**, 5951–5956.

44 C. Filippi, D. J. Singh and C. Umrigar, *Phys. Rev. B: Condens. Matter Mater. Phys.*, 1994, **50**, 14947–14951.

45 J. Qiao, X. Kong, Z.-X. Hu, F. Yang and W. Ji, *Nat. Commun.*, 2014, **5**, 4475.

46 K. Kaasbjerg, K. S. Thygesen and K. W. Jacobsen, *Phys. Rev. B: Condens. Matter Mater. Phys.*, 2012, **85**, 115317.

47 J. Xi, M. Long, L. Tang, D. Wang and Z. Shuai, *Nanoscale*, 2012, **4**, 4348–4369.

48 H. Xie, Y. Qie, M. Imran and Q. Sun, *J. Phys. Chem. A*, 2019, **7**, 14253–14259.

49 S. Grimme, J. Antony, S. Ehrlich and H. Krieg, *J. Chem. Phys.*, 2010, **132**, 154104.

50 J. Liu, S. Wang, Y. Qie, J. Yu and Q. Sun, *Carbon*, 2018, **140**, 680–687.

51 X. Zhang, Z. Yu, S.-S. Wang, S. Guan, H. Y. Yang, Y. Yao and S. A. Yang, *J. Phys. Chem. A*, 2016, **4**, 15224–15231.

52 G. Henkelman, B. P. Uberuaga and H. Jónsson, *J. Chem. Phys.*, 2000, **113**, 9901–9904.

53 I. M. Oleksandr, L. T. Teck and M. Sergei, *Appl. Phys. Express*, 2013, **6**, 027301.

54 V. V. Kulish, O. I. Malyi, M.-F. Ng, P. Wu and Z. Chen, *RSC Adv.*, 2013, **3**, 4231–4236.

55 M. Wagemaker, R. van de Krol, A. P. M. Kentgens, A. A. van Well and F. M. Mulder, *J. Am. Chem. Soc.*, 2001, **123**, 11454–11461.

56 M. V. Koudriachova, N. M. Harrison and S. W. de Leeuw, *Phys. Rev. Lett.*, 2001, **86**, 1275–1278.

57 K. Persson, Y. Hinuma, Y. S. Meng, A. Van der Ven and G. Ceder, *Phys. Rev. B: Condens. Matter Mater. Phys.*, 2010, **82**, 125416.

58 A. Van der Ven, M. K. Aydinol, G. Ceder, G. Kresse and J. Hafner, *Phys. Rev. B: Condens. Matter Mater. Phys.*, 1998, **58**, 2975–2987.

59 M. E. Arroyo y de Dompablo, A. Van der Ven and G. Ceder, *Phys. Rev. B: Condens. Matter Mater. Phys.*, 2002, **66**, 064112.

60 M. K. Aydinol, A. F. Kohan, G. Ceder, K. Cho and J. Joannopoulos, *Phys. Rev. B: Condens. Matter Mater. Phys.*, 1997, **56**, 1354–1365.

61 D. Çakır, C. Sevik, O. Gülseren and F. M. Peeters, *J. Phys. Chem. A*, 2016, **4**, 6029–6035.

62 H. Kim, D. J. Kim, D.-H. Seo, M. S. Yeom, K. Kang, D. K. Kim and Y. Jung, *Chem. Mater.*, 2012, **24**, 1205–1211.

Superflexible C$_{68}$-graphyne as promising anode materials for lithium-ion batteries

Bozhao Wu[1], Xiangzheng Jia[1], Yanlei Wang[2], Jinxi Hu[1], Enlai Gao[1*] and Ze Liu[1*]

[1]Department of Engineering Mechanics, School of Civil Engineering, Wuhan University, Wuhan, Hubei 430072, China.

[2]Beijing Key Laboratory of Ionic Liquids Clean Process, CAS Key Laboratory of Green Process and Engineering, Institute of Process Engineering, Chinese Academy of Sciences, Beijing 100190, China.

*Corresponding authors. Email: enlaigao@whu.edu.cn; ze.liu@whu.edu.cn.

Abstract

The breakthrough in the synthesis of graphyne, graphdiyne and graph-4-yne, stimulates the interest in studying new members of graphyne family for promising applications. In this work, a new allotrope of graphyne with excellent stabilities and ultrahigh specific surface area of 4255 m^2 g^{-1}, named as C_{68}-graphyne, is predicted by first principle calculations. Mechanical tests reveal that C_{68}-graphyne exhibits much smaller in-plane tensile stiffness (~50.5 N m^{-1}) and out-of-plane bending stiffness (~0.5 eV) than those of graphene (in-plane tensile stiffness 350 N m^{-1} and out-of-plane bending stiffness 1.4 eV), suggesting C_{68}-graphyne as a superflexible material. Meanwhile, our results show that monolayer C_{68}-graphyne is a semiconductor with a direct band-gap of 1.0 eV, which can be tuned by strain-engineering, and the calculated carrier mobilities is as high as 1.81×10^5-2.97×10^5 cm^2 V^{-1} s^{-1} at 300 K. Finally, the potential application of C_{68}-graphyne as anode materials for lithium-ion batteries is explored and predicted. The calculated results show a highly efficient charge transfer from the adsorbed Li ions to C_{68}-graphyne yet low diffusion barrier for Li ions in C_{68}-graphyne for fast charge/discharge rate. The storage capacities for Li in monolayer and bilayer C_{68}-graphyne are calculated as high as 1954 and 1675 mA h g^{-1}, respectively. These features make C_{68}-graphyne as promising anode materials for lithium-ion batteries with excellent energy storage capacities as well as fast charge/discharge rates.

1. Introduction

Carbon displays a unique aptitude in constructing various architectures. In the past decades, many carbon allotropes such as carbon fullerenes[1], nanotubes[2] and graphene[3] have been synthesized and characterized. Over thirty years ago, Baughman and Eckhardt predicted two-dimensional (2D) sheets of carbon, called graphyne (GY), including α-, β-, and γ-GY[4]. Among them, γ-GY exhibits high stability and semiconductor feature[5]. With the increasing of acetylenic linkages among adjacent aromatic rings, more members of GY family such as graphdiyne (GDY), graph-3-yne, graph-4-yne and graph-5-yne, were obtained[6]. γ-GY consisting of *sp* and *sp*^{2} carbon atoms, can be viewed as resulting from the substitution of the carbon-carbon bonds in graphene by acetylenic (-C≡C-) linkages. The acetylenic linkage is an efficient connecting unit because of the structural linearity without existing fluctuation arising from cis-trans isomerization[7]. Therefore, the introduced acetylenic linkages create a planar network of γ-GY with high surface area and porosity, making its structural, mechanical, thermal, optical and particularly electrical properties quite different from those of graphene or carbon nanotubes[8-11]. For example, the acetylenic linkages in γ-GY and GDY endow them with significant band-gaps (0.47 and 0.52 eV, respectively)[6]. This is different from graphene, of which the intrinsic zero band-gap significantly limits its practical applications in electronic devices and thus considerable efforts such as increasing thickness[12, 13], introducing substrate[14], chemical doping[15] and tailoring strain[16] have been made to open the band-gap in graphene.

Experimentally, large area GDY was synthesized on the surface of copper via a cross-coupling reaction, showing excellent semiconducting properties[7]. Subsequently, GDY nanotube arrays were also synthesized through an anodic aluminum oxide (AAO) template catalyzed by copper foil[17]. The breakthrough in the synthesis of GDY has stimulated great interest in studying new members of GY family (i.e., γ-GY and graph-4-yne)[18, 19] for promising applications such as hydrogen storage[20, 21] and lithium-ion batteries (LIBs)[22, 23]. For instance, it's reported that the maximum capacity of graph-4-yne for Li storage could reach as high as 947 mA h g^{-1} [19]. It should be noted here that most theoretical studies focus on monolayer materials for uses in LIB anodes, which may

provide a limited view of the performance as the interlayer chemical interaction of these materials in reality is neglected. The interlayer chemical interaction of these materials remains challenging for uses in LIB anode materials and thus their effect on the performance needs to be quantitatively evaluated.

In this work, we report a new member of GY with ultrahigh specific surface area of 4255 m^2 g^{-1} and direct band-gap of 1.00 eV (HSE06), called C_{68}-GY. The stabilities are carefully checked by both phonon dispersion calculations and *ab* initio molecular dynamics (AIMD). The smaller in-plane tensile stiffness ($\sim$50.5 N m^{-1}) and out-of-plane bending stiffness ($\sim$0.5 eV) than those of graphene (in-plane tensile stiffness 350 N m^{-1} and out-of-plane bending stiffness 1.4 eV, respectively) indicate the exceptional flexibility of C_{68}-GY. The calculated highly efficient charge transfer from adsorbed Li ions to C_{68}-GY, low diffusion barrier of Li ions in C_{68}-GY for fast charge/discharge rate, and ultrahigh specific capacity (monolayer: 1954 mA h g^{-1}, bilayer: 1675 mA h g^{-1}) make C_{68}-GY as an ideal candidate of anode materials for LIBs.

2. Computational methods

First principle calculations are carried out in the framework of density functional theory as implemented in the Vienna ab initio simulation package (VASP)[24, 25]. The projector augmented wave method is used to treat the interactions between electrons and irons[26]. General gradient approximation is employed with the Perdew-Burke-Ernzerhof (PBE) functional to describe the exchange and correlation interactions between electrons[27]. The energy cutoff is set to 600 eV for all calculations. The K-points mesh used in the relaxation is $5 \times 5 \times 1$, as well as $11 \times 11 \times 1$ based on Monkhorst-Pack scheme[28] for self-consistent calculations. The cell parameters and ionic positions are fully optimized until the force on each atom is converged below 0.01 eV $Å^{-1}$. In order to avoid interactions between periodic images, a vacuum separation of 30 Å is adopted. The electronic properties are calculated by both using PBE and hybrid functionals (HSE06)[29]. Density functional perturbation theory[30] calculations are performed to obtain the phonon dispersion combining VASP and the open source code Phonopy[31].

3. Results and discussion

3.1. Structure and chemical analysis

Similar to γ-GY (**Fig. S1**), the new form of GY consists of acetylenic linkages and aromatic rings as shown in **Fig. 1a**. The primitive cell contains 24 carbon atoms (**Fig. 1b**). The optimized lattice constant (10.84 Å) is larger than that of γ-GY (6.86~6.89 Å), but C_{68}-GY has the same hexagonal symmetry (P6/mmm: D_{6h}) as γ-GY[4-6]. From **Fig. 1a**, each two acetylenic linkages concurrently join to the neighboring aromatic rings resulting in an octatomic ring. Besides, the angles between acetylenic linkages and aromatic rings are obtuse (α_1=125.8°), differing from those in GY (60°). According to the previous naming convention of GY[32], this new GY is named as C_{68}-GY. As we know, there're three types of C-C bonds in γ-GY (**Fig. S1b**): sp^2-sp^2 (B_1=1.436 Å), sp^2-sp (B_2=1.408 Å) and sp-sp (B_3=1.223 Å)[5]. While there are four types of C-C bonds in C_{68}-GY (**Fig. 1b**): sp^2-sp^2 (B_1=1.462 Å and B_2=1.397 Å), sp^2-sp (B_3=1.413 Å) and sp-sp (B_4=1.227 Å). For further insights into the bond characteristics, total electron densities of C_{68}-GY are plotted (**Fig. 1c**). The electron densities of sp-sp bonds (B_4) are obviously higher than others, suggesting stronger electron delocalization in the sp-sp bonds (**Fig. 1d**). The linkages between the aromatic rings and acetylene union of C_{68}-GY are of obtuse angle (α_2 =155.8°), which is attributed to the electrostatic repulsive interactions between two adjacent acetylenic linkages in the same octatomic ring. Meanwhile, the interactions further stretch the shared bonds (B_1) between octatomic and aromatic rings, thus resulting the bond B_1 longer than B_2, which accounts for two types of sp^2-sp^2 bonds in aromatic rings. Meanwhile, the octatomic and aromatic rings together form a pore with the diameter of 8.22 Å (**Fig. 1a**), much larger than those in graph-n-yne (n = 1, 2, 3, 4, 5)[33]. In particular, the theoretical specific surface area is 4255 m² g^{-1}, larger than activated carbon (~2000 m² g^{-1})[34] and graphene (experimental data: ~1500 m² g^{-1}, theoretical calculation: ~2620 m² g^{-1})[35], indicating its potential application for gas adsorption and purification. Besides, two methods are used to determine the Van der Waals (vdW) thickness of monolayer C_{68}-GY by characterizing the weak interlayer interactions of C_{68}-GY. The first one is to calculate the energy curve for two separated C_{68}-GY versus the different distances (**Fig. 2a**), from which we find that the equilibrium

distance of d_{vdW} is 3.76 Å with the adhesion energy of 104.3 mJ/m^2. The other method is to fully optimize C$_{68}$-GY bilayer with an initial separation of 4 Å. The optimized energy of bilayer C$_{68}$-GY is compared with monolayer C$_{68}$-GY to obtain the adhesion energy of 106.6 mJ m^{-2}. The smaller adhesion energy of 104.3-106.6 mJ m^{-2} found here than that of γ-GY (223.5 mJ m^{-2})[9] is attributed to the sparser distribution of in-plane carbon atoms.

3.2. Stability

Firstly, the thermal stability of C$_{68}$-GY with respect to its cohesive energy is evaluated. According to **Eq. (1)**, the cohesive energy is determined to be 7.09 eV per atom.

$$E_{\text{coh}} = \frac{24E_{\text{C}} - E_{\text{C}_{68}\text{-GY}}}{24} \tag{1}$$

where E_{C} and $E_{\text{C}_{68}\text{-GY}}$ denote the energy of the isolated carbon atom and C$_{68}$-GY. Comparing with GY and graphene (**Fig. 2b**), the stability of C$_{68}$-GY closely follows γ-GY (7.21 eV)[5] and graphene (8.11 eV)[36]. Afterwards, the dynamic stability of C$_{68}$-GY is verified by phonon dispersion calculation, where the absence of imaginary modes[37] indicates the dynamical stability of C$_{68}$-GY monolayer (**Fig. 2c**). Meanwhile, the thermodynamic stability in a supercell (2×2×1) is evaluated by performing AIMD simulations at 300 K for 10 ps. The temperature is controlled by using the Nosé-Hoover thermostat. During the AIMD simulation, the C$_{68}$-GY upholds its structural integrity with only slight corrugation because of thermal fluctuations (**Fig. 2d**). Subsequently, we probe the chemical stability of C$_{68}$-GY under ambient conditions with common molecules in the atmosphere (the molecular ratio is set as N$_2$:O$_2$:H$_2$O:H$_2$=22:6:3:3 to mimic atmosphere conditions) for 10 ps in the NPT ensemble with controlled temperature of 300 K and pressure of 0 bar. Slight fluctuation of lattice constants (**Fig. S2a**) and no bonds formed or broken during the whole AIMD simulations (**Fig. 2e-f**) suggest the great chemical stability of C$_{68}$-GY under ambient conditions. The above results confirm the remarkable energetic, dynamical, thermodynamic and chemical stabilities of C$_{68}$-GY. In addition, recently GDY and graph-4-yne have been successfully synthesized on the surface of the copper foil[7, 19], thus C$_{68}$-GY could be expected to be grown on copper substrate.

3.3. Mechanical properties

To investigate the mechanical properties of C_{68}-GY, tensile tests for monolayer C_{68}-GY in rectangle cell are performed (**Fig. 3a-b**). The uniaxial stress-strain in **Fig. 3c** shows that the tensile strength (σ) along x- and y-directions are 21.7 N m^{-1} (58.0 GPa, using the thickness of 3.74 Å for monolayer C_{68}-GY) and 14.7 N m^{-1} (39.3 GPa), corresponding to the failure strain of 32% and 20%, respectively. The larger failure strain along x-direction is attributed to some acetylenic linkages directly bearing tensile load. Similar to graphene[38, 39], C_{68}-GY has almost isotropic in-plane elastic response with in-plane tensile stiffness ~50.5 N m^{-1}, which is smaller than those of graphene (350 N m^{-1}, 1050 GPa)[39]. Note that, as $\varepsilon_x = 25\%$, the stress-strain and strain energy-strain responses abruptly change, implying the atomic structure of C_{68}-GY has a significant transformation. As shown in **Fig. 3b**, we find that only the acetylenic linkages directly bear load along x-direction, and other acetylenic linkages are broken and then reconstructed. In addition to in-plane mechanical behaviors, we also examine its out-of-plane elasticity, i.e. bending stiffness D. Two methods can be used to calculate D. The first one is to fit the bending energy per unit area E_{ben} of a C_{68}-GY nanotube as a function of its radius R, based on the equation $E_{ben} = DR^{-2}/2$[40]; The second one is to fit the phonon dispersions $\omega(q)$ with the equation $\omega^2=(D/\rho)q^4$ according to the quadratic dispersion of flexural phonon mode ZA[41], where ρ is the areal density of C_{68}-GY (4.70×10^{-7} kg m^{-2}). Due to the first method requiring high computational costs, thus the second approach is adopted in this work (**Fig. S2b**). The calculated D along Γ-M and Γ-K are both ~0.50 eV. In the same way, D = 1.43 eV for graphene is calculated (**Fig. S2c**), coinciding with previous DFT calculations (1.44 eV)[42]. Moreover, the comparison of mechanical properties with other typical carbon allotropes is listed in **Table S1**. The small in-plane tensile stiffness and out-of-plane bending stiffness render C_{68}-GY as an atomic membrane with exceptional flexibility.

3.4. Electronic properties

The band structure and projected density of state (PDOS) are computed with PBE functional. Unlike γ-GY (at M point)[43], the conduction band minimum (CBM) and valence band maximum (VBM) of C_{68}-GY locate at the K point in the Brillouin zone. The band-gap of 0.51 eV (**Fig. 4a**)

is larger than that of γ-GY (0.46 eV)[5]. From the PDOS (**Fig. S3a**), only contribution of p_z orbitals is found around the Fermi level (-1.3 eV to 2.6 eV). Therefore, only bands corresponding to π and π^* states are presented in this gap. Because the PBE functional tends to underestimate the band-gaps of materials[44], more reliable method with HSE06 functional is used to recompute band structure (E_g = 1.00 eV) as depicted in **Fig. 4b**. Furthermore, we calculate the effective masses utilizing the expression:

$$m^* = \frac{h^2}{\partial^2 E / \partial k^2} \tag{2}$$

The $|m^*|$ values along the K-M direction are larger than those along the K-Γ direction. Meanwhile, biaxial strain (ε) ranging from -10% to 10% is used to tune the electronic properties of C_{68}-GY. The band-gap E_g, strain energy, as well as the effective masses for electrons and holes are calculated corresponding to the strain (**Fig. 4c** and **Table S2**). The E_g and $|m^*|$ both increase with the increasing of strain. As ε = 10%, the E_g increases to be 0.88 eV. During the compression, the E_g firstly decreases and then increases. Whereas, the band structures show an indirect feature as C_{68}-GY is further compressed to ε of about -8% (**Fig. S4**). Meanwhile, the strain energies abnormally decrease at ε of about -8%, implying the structures substantially change. We check the structures corresponding to this critical strain and confirm that a phase transition occurs, in which the original octatomic rings reconstruct to be tetratomic and new octatomic rings (**Fig. 4d**). Finally, the carrier mobilities of C_{68}-GY are given by[45]:

$$\mu_{2D} = \frac{e h^3 C_{2D}}{k_B T \left| m^* \right| m_d (E_1)^2} \tag{3}$$

where m_d is averaged effective mass determined by $\sqrt{m_x^* m_y^*}$, m_x^* and m_y^* are the effective mass (m^*) along transporting x and y directions, respectively, C_{2D} is the elastic constant and E_1 is the DP constant (**Fig. S5**). C_{2D} can be determined by the calculations of elastic constant matrix of monolayer C_{68}-GY. Hence, the carrier mobilities along x- and y-directions are obtained (**Table 1**). For monolayer C_{68}-GY at room temperature (300 K), the carrier mobility is as high as 1.81×10^5-

2.97×10^5 cm^2 V^{-1} s^{-1}, which is much higher compared to other 2D materials such as MoS$_2$[46] and black phosphorene[45]. The high carrier mobility mainly originates from the small deformation potential (0.4 eV) that is much smaller than that of graphene (5.0 eV)[47], MoS$_2$ (3.9 eV)[46] and phosphorene (2.7 eV)[45]. The tunable electronic structure and excellent electronic conductance make C$_{68}$-GY a promising candidate for future flexural electronic devices.

3.5. The application of C$_{68}$-GY as the anode materials for lithium-ion batteries

The promising application of C$_{68}$-GY as the anode materials for LIBs is investigated in this part. Firstly, the strongest adsorption site for an isolated Li on C$_{68}$-GY monolayer ($2 \times 2 \times 1$) is determined by evaluating the adsorption energy E_{ad}:

$$E_{ad} = \frac{E(m@C_{68}\text{-GY}) - E(C_{68}\text{-GY}) - m\mu(\text{Li})}{m} \tag{4}$$

where $E(C_{68}$-GY$)$ and $E(m@C_{68}$-GY$)$ are the total energies of C$_{68}$-GY before and after adsorbing m Li ions, respectively, and $\mu(\text{Li})$ is the chemical potential of Li[48]. Five intercalation positions denoted as S1-S5 are considered (**Fig. 5a**). DFT-D3 method of Grimme is employed for the corrections of the van der Waals interactions[49]. The results show the most favorite site of Li adsorbed on C$_{68}$-GY is S4 with the lowest E_{ad} of -3.01 eV (**Table 2**). The absolute values of adsorptions energies are all larger than that of graphite (-0.78 eV)[50], suggesting a strong ionic binding between Li ions and the C$_{68}$-GY substrate. The charge density difference is plotted as depicted in **Fig. 5c-e**, showing that Li is ionized as adsorbed on the surface of C$_{68}$-GY. This observation coincides with the Bader charge analysis revealing that Li transfers charges of 0.91 e (S1), 0.98 e (S3) and 0.92 e (S4) to the C$_{68}$-GY, respectively, approaching to that of MoN$_2$ (0.89 e)[51]. These results clearly demonstrate that Li ion is in the cationic state with chemically adsorbed onto C$_{68}$-GY monolayer. Moreover, PDOS calculations (**Fig. S3b-d**) clearly show the metallic characters of C$_{68}$-GY adsorbed one Li, arising from p_z orbitals around the Fermi level to the left. The excellent electrical conduction is of significance for the anode materials.

Besides, the charge/discharge rate is of great importance for the performance of anode materials,

which depends upon the mobility of ions. Therefore, we probe the diffusion behaviors of Li ions over and through the C_{68}-GY using the climbing-image nudged elastic band (CI-NEB) method[52]. For the in-plane diffusion, the diffusion paths of P1, P2, P3 and P4 are considered (**Fig. 5b**). Among, P1 and P2 are the paths that Li migrates from the most favorite site (S4) to another one. For the out-of-plane diffusion paths, P5 denotes the path passing through S1 (octatomic ring) from one side to another. The diffusion barriers of ion over and through monolayer C_{68}-GY are shown in **Fig. 5f-g**, involving the low diffusion barriers of 0.13 eV, 0.25 eV and 0.45 eV for the P1, P3 and P4, respectively. For the out-of-plane diffusion, P5 uncovers the highest diffusion barrier of 3.14 eV. It can be understood that the small pore size of octatomic ring results in a larger repulsive Coulomb interaction, which significantly enhances the diffusion barrier. These diffusion barriers of in-plane diffusion are smaller than those of the well-studied electrode materials, such as bulk silicon (0.57 eV)[53, 54] and TiO_2-based polymorphs (0.65 eV)[55, 56]. To further probe the effect of interlayer chemical interaction on the diffusion properties, we calculate the diffusion path of P1 (**Fig. 5b**) for bilayer C_{68}-GY (**Fig. S6a**) with the barrier of 8.4 meV. From the barrier profile, the state at coordinate 3 is more stable than initial/final state (Li on S4). Conversely, it can be speculated that the barrier of Li diffusing from coordinate 3 to transition state (TS) is 57 meV (**Fig. S6b**). Compared to the diffusion barriers of Li on monolayer, the weak interlayer vdW interaction reduces the diffusion barriers and alters the most favorite site where Li intercalated in C_{68}-GY.

Furthermore, we evaluate the Li concentration intercalated in C_{68}-GY to determine the specific capacity for Li storage. The specific capacity is calculated by:

$$C = \frac{xF}{M} \qquad (5)$$

where x is the concentration of Li ions in C_{68}-GY (the ratio between intercalated Li ions and carbon atoms in the hybrid system), F denotes the Faraday constant 26.8 Ah mol^{-1}, and M is the mass of carbon atoms. To explore the stabilities of intermediate product (Li_xC) with various Li ion concentrations (x), the formation energy is calculated to plot the convex hull. There are two methods used to calculate the formation energy[57-59]. The first one is to use metallic Li and non-

lithiated C_{68}-GY as reference states; the second one is to use non-lithiated C_{68}-GY and the fully lithiated C_{68}-GY as reference states. Herein the second method is adopted, and the formation energy of Li_xC is calculated by:

$$E_{form} = E - x \times E_{LiC} - (1-x) \times E_C \qquad (6)$$

where E is the total energy of the configuration per $Li_x\varnothing_{1-x}C$ formula unit ($0 < x < 1$), E_{LiC} is the energy of LiC, and E_C is the energy of C_{68}-GY per carbon atom. **Fig. 6a** displays the formation energies for Li_xC with varying Li concentrations for monolayer C_{68}-GY. AIMD simulations for the configurations of LiC are performed under NPT ensemble with temperature of 300 K and pressure of 0 bar to investigate the thermodynamic stability (**Fig. S7a**). After running for 10 ps, LiC still holds the structural integrity but with corrugations leading lattice contraction within the range of -5% (**Fig. S7b**) accompanying with some of the original octatomic rings reconstruct to be tetratomic and new octatomic rings, indicating a phase transition (**Fig. S7c-d**). Besides, the volume expansion or contraction is considered during the adsorption process which is a key parameter controlling whether electrode reactions are reversible. As we known, the volume is not easy to be identified for 2D materials. Instead, the in-plane expansion or contraction is considered using the lattice constant (a) ratio, which can be calculated by a/a_0, where a_0 and a are the lattice constants of C_{68}-GY before and after adsorbing Li ions, respectively. Along these structures with the minimum formation energy (**Fig. 6a,** green points) as depicted in **Fig. S8**, the adsorption energy and lattice changes are calculated as shown in **Fig. S9a**. The negative adsorption energies demonstrate these adsorption processes are exoergic without forming Li clusters. Tiny lattice changes of C_{68}-GY manifest that the intercalation of Li ions weakly influences the in-plane expansion or contraction. On the one hand, with the increase of Li ions intercalated in C_{68}-GY, the repulsive electrostatic interactions between Li ions will induce the in-plane lattice expansion (**Fig.S8a-b**). On the other hand, the C_{68}-GY with weak out-of-plane resistance is apt to be corrugated if Li ions asymmetrically distribute on C_{68}-GY (**Fig. S8c-d**), which thus results in the in-plane contraction of the system. These two competitive mechanisms explain the trend of lattice constant changes. For Li intercalated in bilayer C_{68}-GY, three configurations with varying Li

Journal of Materials Chemistry A Accepted Manuscript

concentrations (**Fig. S8e-g**) are probed with the negative adsorption energies (**Table 3**). Meanwhile, the calculated formation energies further manifest the intermediate configurations with Li ions intercalated in bilayer C_{68}-GY are also stable.

Afterwards, the OCV profiles are calculated, which is a measurement of the performance of anode materials for LIBs. The charge/discharge processes of C_{68}-GY follow the half-cell reaction vs Li/Li$^+$:

$$Lix_2C+(x_1-x_2)Li^+ +(x_1-x_2)e^{-1} \leftrightarrow Lix_1C \tag{7}$$

where $x_1 > x_2$. Then the voltage is:

$$V = -\frac{G(Lix_1C)-G(Lix_2C)-(x_1-x_2)G(Li)}{(x_1-x_2)ze} \tag{8}$$

where G is the Gibbs free energy of the compound, $\Delta x = x_1 - x_2$ ($x_1 > x_2$) and z represents the charge of metal ion (here $z = 1$ for Li). Since the contribution of entropy ($T\Delta S \approx 25$ meV at 300K) and enthalpy ($P\Delta V$ in the order of 1.0^{-5} eV) can be neglected[60], the Gibbs free energy ($\Delta G = \Delta E + P\Delta V - T\Delta S$) can be approximated as the internal energy ΔE[61]. Within this approximation, the voltage profiles are calculated along these structures with minimum formation energy (**Fig. 6a**)[62]. From the voltage profile (**Fig. 6b**), as x increases to 0.875, corresponding to a specific capacity of 1954 mA h g^{-1}, the voltage decreases to 0.14 V. As x approaches to 1.0, the voltage would decrease to -0.54 V, indicating the lithiation process will stop. Similarly, for Li intercalations in bilayer C_{68}-GY, the calculated voltage is 0.37 V when x increases to 0.75, corresponding to the capacity of 1675 mA h g^{-1}. As x increases to 1.125, the voltage of $Li_{1.125}C$ decreases to -0.11 V. Besides, the comparisons of the specific capacities of C_{68}-GY with other typical carbon allotropes are shown in **Fig. S9b**, indicating C_{68}-GY is an ideal candidate as the anode materials for LIBs with high specific capacity.

4. Conclusion

In this work, we predict a novel allotropy of GY using first principle calculations, named as C_{68}-

GY. The remarkable energetic, dynamical, thermodynamic and chemical stabilities of C_{68}-GY are confirmed by the first principle calculations. The unique atomic structures endow it with ultrahigh specific surface area (4255 m^2 g^{-1}), high ductility (20%-30%) and excellent elastic flexibility (in-plane tensile stiffness ~50.5 N m^{-1} and out-of-plane bending stiffness ~0.5 eV). The calculated electronic structure shows a direct gap in the band structure (0.51 eV and 1.00 eV at PBE and HSE06 levels, respectively). The tuneability of the band structure by strain-engineering is further explored. The direct band-gap is observed increasing with increasing strain. The calculated high carrier mobilities of 1.81×10^5-2.97×10^5 cm^2 V^{-1} s^{-1} indicate the potential applications of C_{68}-GY in electronic devices. Finally, C_{68}-GY possesses the low diffusion energy barrier of 0.13~0.45 eV for fast charge/discharge rates as well as high specific capacities (monolayer: 1954 mA h g^{-1}, bilayer: 1675 mA h g^{-1}). These exceptional electrical conductivity, fast charge/ discharge rates and high capacity suggest that C_{68}-GY can be utilized as promising anode materials for LIBs with high performance.

Conflicts of interest

There are no conflicts to declare.

Acknowledgement

References

1. H. W. Kroto, J. R. Heath, S. C. O'Brien, R. F. Curl and R. E. Smalley, *Nature*, 1985, **318**, 162-163.

2. S. Iijima, *Nature*, 1991, **354**, 56-58.

3. K. S. Novoselov, A. K. Geim, S. V. Morozov, D. Jiang, Y. Zhang, S. V. Dubonos, I. V. Grigorieva and A. A. Firsov, *Science*, 2004, **306**, 666-669.

4. R. Baughman, H. Eckhardt and M. Kertesz, *The Journal of Chemical Physics*, 1987, **87**, 6687-6699.

5. A. R. Puigdollers, G. Alonso and P. J. C. Gamallo, *Carbon*, 2016, **96**, 879-887.

6. N. Narita, S. Nagai, S. Suzuki and K. Nakao, *Physical Review B*, 1998, **58**, 11009-11014.

7. G. Li, Y. Li, H. Liu, Y. Guo, Y. Li and D. Zhu, *Chemical Communications*, 2010, **46**, 3256-3258.

8. Y. Zhang, Q. Pei and C. Wang, *Applied Physics Letters*, 2012, **101**, 081909.

9. S. W. Cranford and M. J. Buehler, *Carbon*, 2011, **49**, 4111-4121.

10. J. Kang, J. Li, F. Wu, S.-S. Li and J.-B. Xia, *The Journal of Physical Chemistry C*, 2011, **115**, 20466-20470.

11. T. Ouyang, Y. Chen, L.-M. Liu, Y. Xie, X. Wei and J. Zhong, *Physical Review B*, 2012, **85**, 235436.

12. Y. Zhang, T.-T. Tang, C. Girit, Z. Hao, M. C. Martin, A. Zettl, M. F. Crommie, Y. R. Shen and F. J. N. Wang, *Nature*, 2009, **459**, 820-823.

13. E. V. Castro, K. Novoselov, S. Morozov, N. Peres, J. L. Dos Santos, J. Nilsson, F. Guinea, A. Geim and A. C. J. P. r. l. Neto, *Physical Review Letters*, 2007, **99**, 216802.

14. S. Y. Zhou, G. H. Gweon, A. V. Fedorov, P. N. First, W. A. de Heer, D. H. Lee, F. Guinea, A. H. Castro Neto and A. Lanzara, *Nature Materials*, 2007, **6**, 770-775.

15. W. Zhang, C.-T. Lin, K.-K. Liu, T. Tite, C.-Y. Su, C.-H. Chang, Y.-H. Lee, C.-W. Chu, K.-H.

Journal of Materials Chemistry A Accepted Manuscript

Wei, J.-L. Kuo and L.-J. Li, *ACS Nano*, 2011, **5**, 7517-7524.

16. G. Gui, J. Li and J. J. P. R. B. Zhong, *Physical Review B*, 2008, **78**, 075435.

17. G. Li, Y. Li, X. Qian, H. Liu, H. Lin, N. Chen and Y. Li, *The Journal of Physical Chemistry C*, 2011, **115**, 2611-2615.

18. Q. Li, Y. Li, Y. Chen, L. Wu, C. Yang and X. Cui, *Carbon*, 2018, **136**, 248-254.

19. J. Gao, J. Li, Y. Chen, Z. Zuo, Y. Li, H. Liu and Y. Li, *Nano Energy*, 2018, **43**, 192-199.

20. S. Kumar, Dhilip Kumar Thogluva Janardhanan, *ACS Applied Materials & Interfaces*, 2017, **9**, 28659-28666.

21. H. J. Hwang, Y. Kwon and H. Lee, *The Journal of Physical Chemistry C*, 2012, **116**, 20220-20224.

22. H. Zhang, M. Zhao, X. He, Z. Wang, X. Zhang and X. Liu, *The Journal of Physical Chemistry C*, 2011, **115**, 8845-8850.

23. H. J. Hwang, J. Koo, M. Park, N. Park, Y. Kwon and H. Lee, *The Journal of Physical Chemistry C*, 2013, **117**, 6919-6923.

24. G. Kresse and J. Hafner, *Physical Review B*, 1994, **49**, 14251-14269.

25. G. Kresse and J. Furthmüller, *Physical Review B*, 1996, **54**, 11169-11186.

26. P. E. Blöchl, *Physical Review B*, 1994, **50**, 17953-17979.

27. J. P. Perdew, K. Burke and M. Ernzerhof, *Physical Review Letters*, 1996, **77**, 3865-3868.

28. H. J. Monkhorst and J. D. Pack, *Physical Review B*, 1976, **13**, 5188-5192.

29. J. Heyd, G. E. Scuseria and M. Ernzerhof, *The Journal of Chemical Physics*, 2003, **118**, 8207-8215.

30. S. Baroni, S. De Gironcoli, A. Dal Corso and P. Giannozzi, *Reviews of Modern Physics*, 2001, **73**, 515-562.

31. A. Togo and I. Tanaka, *Scripta Materialia*, 2015, **108**, 1-5.

32. H. Lu and S.-D. Li, *Journal of Materials Chemistry C*, 2013, **1**, 3677-3680.

33. S. Lin and M. J. Buehler, *Nanoscale*, 2013, **5**, 11801-11807.

34. S. Y. Lu, M. Jin, Y. Zhang, Y. B. Niu, J. C. Gao and C. M. Li, *Advanced Energy Materials*, 2018, **8**, 1702545.

35. Z.-S. Wu, G. Zhou, L.-C. Yin, W. Ren, F. Li and H.-M. Cheng, *Nano Energy*, 2012, **1**, 107-131.

36. V. O. Özçelik and S. Ciraci, *The Journal of Physical Chemistry C*, 2013, **117**, 2175-2182.

37. Y. Li, Y. Liao and Z. Chen, *Angewandte Chemie International Edition*, 2014, **53**, 7248-7252.

38. X. Wei, B. Fragneaud, C. A. Marianetti and J. W. Kysar, *Physical Review B*, 2009, **80**, 205407.

39. F. Liu, P. Ming and J. Li, *Physical Review B*, 2007, **76**, 064120.

40. Z. Zhang, Y. Yang, E. S. Penev and B. I. Yakobson, *Advanced Functional Materials*, 2017, **27**, 1605059.

41. L. J. Karssemeijer and A. Fasolino, *Surface Science*, 2011, **605**, 1611-1615.

42. Y. Wei, B. Wang, J. Wu, R. Yang and M. L. Dunn, *Nano Letters*, 2013, **13**, 26-30.

43. K. Srinivasu and S. K. Ghosh, *The Journal of Physical Chemistry C*, 2012, **116**, 5951-5956.

44. C. Filippi, D. J. Singh and C. Umrigar, *Physical Review B*, 1994, **50**, 14947-14951.

45. J. Qiao, X. Kong, Z.-X. Hu, F. Yang and W. Ji, *Nature Communications*, 2014, **5**, 4475.

46. K. Kaasbjerg, K. S. Thygesen and K. W. Jacobsen, *Physical Review B*, 2012, **85**, 115317.

47. J. Xi, M. Long, L. Tang, D. Wang and Z. Shuai, *Nanoscale*, 2012, **4**, 4348-4369.

48. H. Xie, Y. Qie, M. Imran and Q. Sun, *Journal of Materials Chemistry A*, 2019, **7**, 14253-14259.

49. S. Grimme, J. Antony, S. Ehrlich and H. Krieg, *The Journal of Chemical Physics*, 2010, **132**, 154104.

50. J. Liu, S. Wang, Y. Qie, J. Yu and Q. Sun, *Carbon*, 2018, **140**, 680-687.

51. X. Zhang, Z. Yu, S.-S. Wang, S. Guan, H. Y. Yang, Y. Yao and S. A. Yang, *Journal of Materials Chemistry A*, 2016, **4**, 15224-15231.

52. G. Henkelman, B. P. Uberuaga and H. Jónsson, *The Journal of Chemical Physics*, 2000, **113**,

9901-9904.

53. I. M. Oleksandr, L. T. Teck and M. Sergei, *Applied Physics Express*, 2013, **6**, 027301.

54. V. V. Kulish, O. I. Malyi, M.-F. Ng, P. Wu and Z. Chen, *RSC Advances*, 2013, **3**, 4231-4236.

55. M. Wagemaker, R. van de Krol, A. P. M. Kentgens, A. A. van Well and F. M. Mulder, *Journal of the American Chemical Society*, 2001, **123**, 11454-11461.

56. M. V. Koudriachova, N. M. Harrison and S. W. de Leeuw, *Physical Review Letters*, 2001, **86**, 1275-1278.

57. K. Persson, Y. Hinuma, Y. S. Meng, A. Van der Ven and G. Ceder, *Physical Review B*, 2010, **82**, 125416.

58. A. Van der Ven, M. K. Aydinol, G. Ceder, G. Kresse and J. Hafner, *Physical Review B*, 1998, **58**, 2975-2987.

59. M. E. Arroyo y de Dompablo, A. Van der Ven and G. Ceder, *Physical Review B*, 2002, **66**, 064112.

60. M. K. Aydinol, A. F. Kohan, G. Ceder, K. Cho and J. Joannopoulos, *Physical Review B*, 1997, **56**, 1354-1365.

61. D. Çakır, C. Sevik, O. Gülseren and F. M. Peeters, *Journal of Materials Chemistry A*, 2016, **4**, 6029-6035.

62. H. Kim, D. J. Kim, D.-H. Seo, M. S. Yeom, K. Kang, D. K. Kim and Y. Jung, *Chemistry of Materials*, 2012, **24**, 1205-1211.

Figures, Tables, and Captions
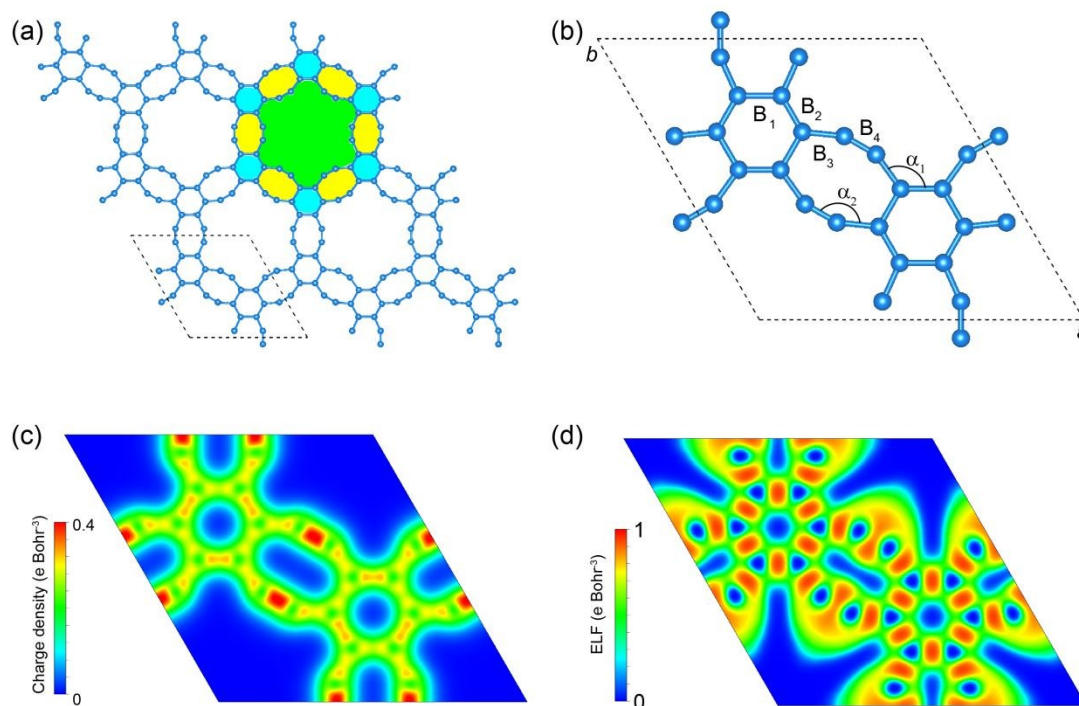
Fig. 1 (a) Schematic diagram of C_{68}-GY, and (b) its primitive cell. Color coding consists of yellow for octatomic rings, cerulean for aromatic rings, and green for the pores. B_1, B_2, B_3 and B_4 denote the different bonds, and α_1 and α_2 are two angles. The plotted iso-surfaces of (c) total electron density and (d) electron location function (ELF) are shown in the primitive cell.
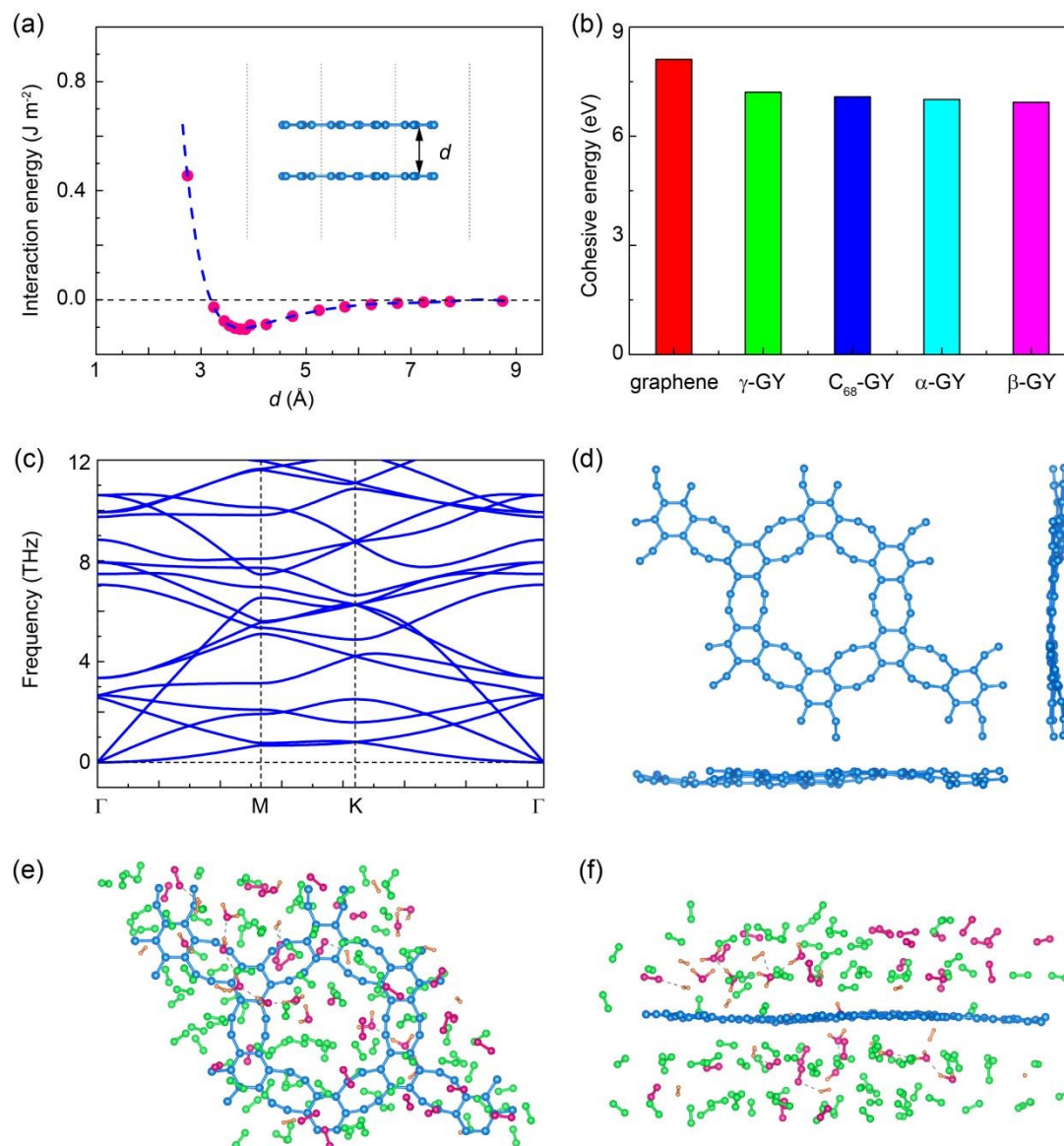
Fig. 2 (a) The interaction energy as a function of various separation d, between two layers of C_{68}-GY (inset). The blue dash line denotes the fitting curve for the red points. (b) The comparation of cohesive energies of graphene, α-, β-, and γ-GY with C_{68}-GY. The data for graphene, α-GY, β-GY and γ-GY in are obtained from **Refs. 5, 36**. (c) The calculated phonon dispersion spectrum of C_{68}-GY. (d) the snapshots (top and side views) taken from AIMD simulations of C_{68}-GY. (e-f) the snapshots (top and side views) taken from AIMD simulations of C_{68}-GY under the atmosphere, where the ratio of the molecular numbers is set to be $N_2:O_2:H_2O:H_2=22:6:3:3$ and the blue, red, green and orange spheres represent C, O, N and H atoms, respectively.
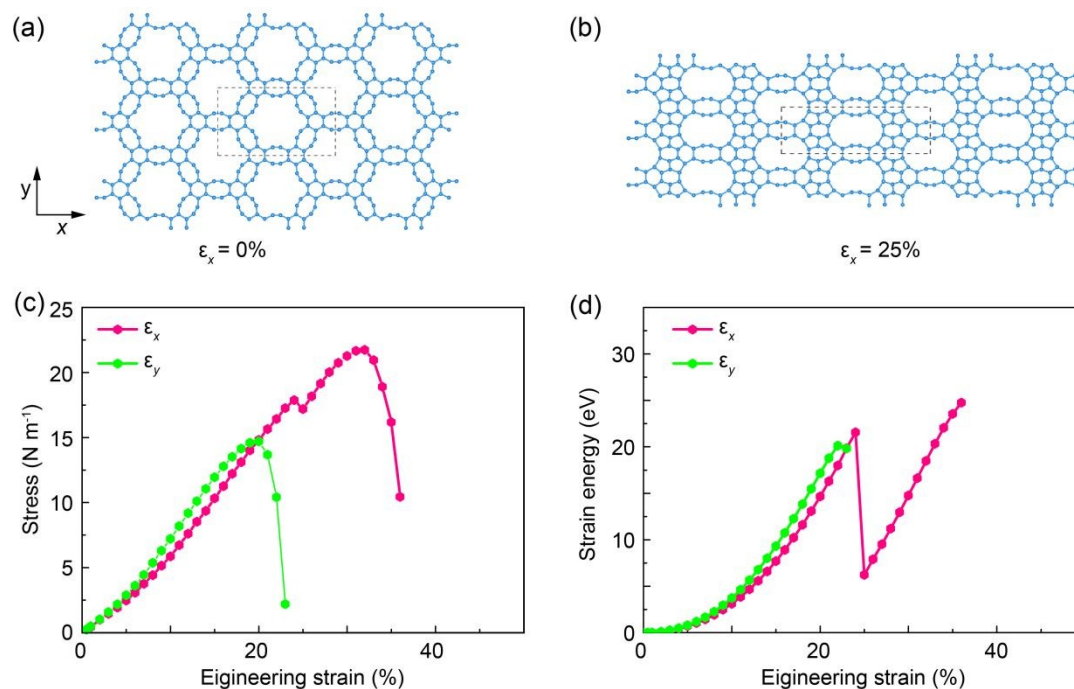
Fig. 3 (a) The schematic diagram of uniaxial tensile tests using rectangular cell (dash line); (b) the atomic configuration under uniaxial tension of ε_x = 25%; (c) The stress and (d) strain energy responses under the uniaxial tension.
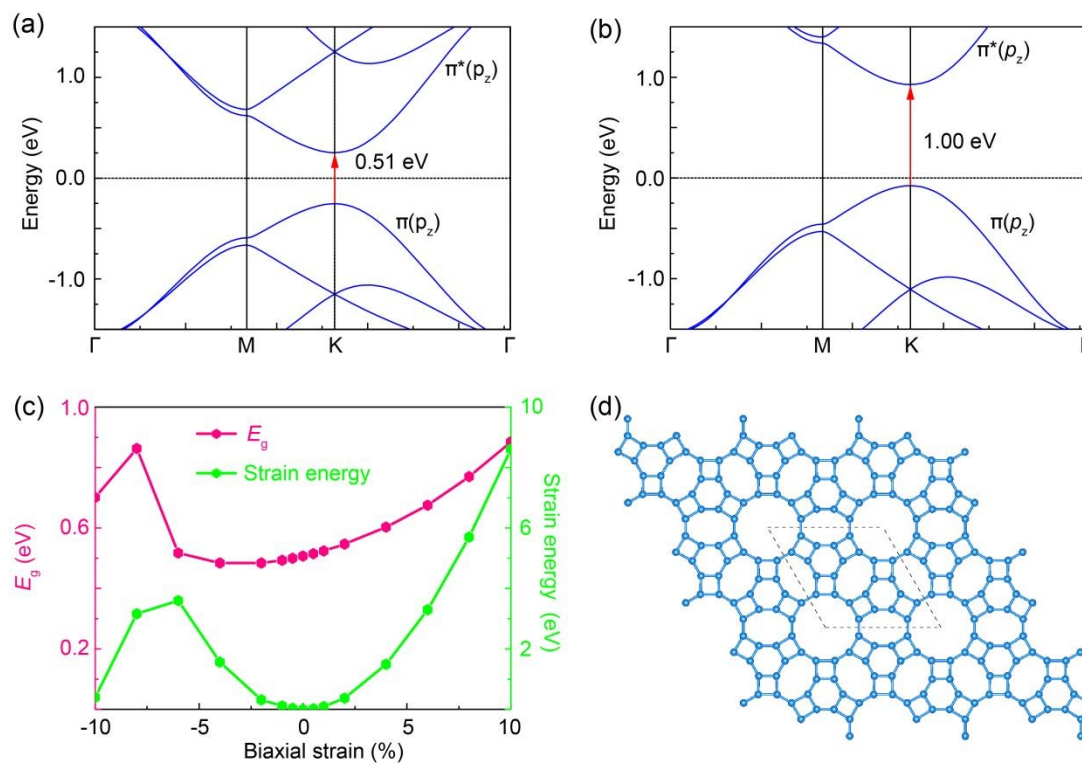
Fig. 4 Band structure of C_{68}-GY monolayer are calculated by using (a) PBE and (b) HSE06 functionals following the path Γ-M-K-Γ of the first Brillouin zone. (c) The calculated band-gap E_g and strain energy under different biaxial strain. (d) The atomic configuration of the C_{68}-GY at biaxial strain of -8%.
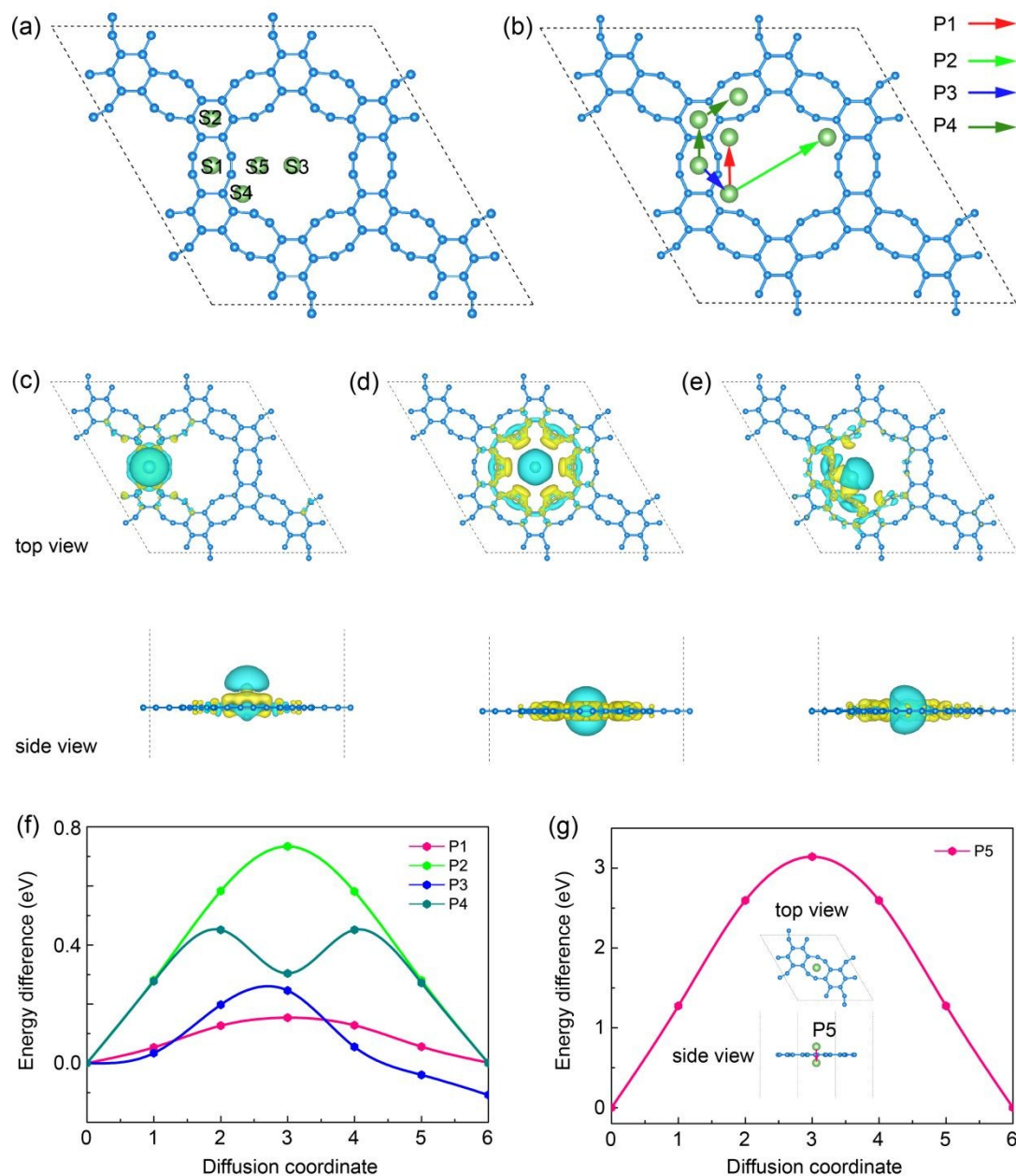
Fig.5 (a) Five potential different adsorption sites of an intercalated Li ion in C_{68}-GY monolayer, and the blue and green spheres represent C and Li atoms, respectively. (b) Schematics of the diffusion P1 to P4 (top view). Top and side views of the differential charge density of one Li ion adsorbed on (c) S1, (d) S3 and (e) S4 with an isosurface value of 0.0006 e Bohr^{-3}. Color coding consists of yellow for charge gain and green for charge loss. The diffusion barrier profiles of (f) in-plane diffusion (P1-P4) and (g) the out-plane diffusion (P5).
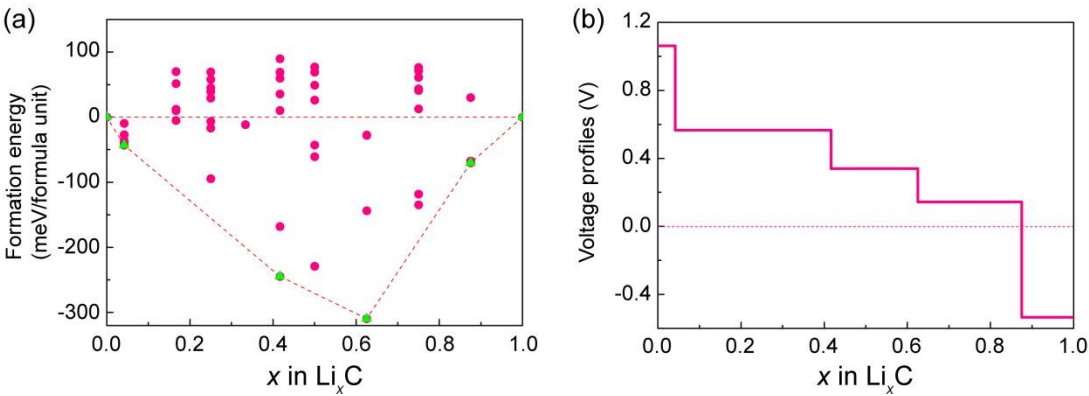
Fig. 6 (a) Formation energies calculated for different configurations of C_{68}-GY intercalated Li ions; (b) The calculated voltage profile along the minimum energy path of formation energies, green points of (a).

Table 1 The calculated carrier mobility μ_{2D} at 300 K for monolayer C_{68}-GY along the x- and y-directions, including the in-plane elastic constants C_{2D}, DP constant, E_1 and effective mass m^*.

Carrier type	m_x^*/m_0	m_y^*/m_0	E_{1x}	E_{1y}	C_{2D_x}	C_{2D_y}	μ_{2D_x}	μ_{2D_y}
			(eV)		(N m^{-1})		(10^5 cm^2 V^{-1} s^{-1})	
electron	0.214	0.185	0.382	0.406	78.202	78.202	2.681	2.745
hole	-0.223	-0.193	-0.446	-0.374	78.202	78.202	1.810	2.974

Table 2 The adsorption energy (E_{ad}) and height (h) for the five different adsorption sites in supercell ($2\times2\times1$) of monolayer C_{68}-GY.

monolayer	Sites	E_{ad} (eV)	h (Å)*
$2\times2\times1$	S1	-2.90	1.67
	S2	-2.62	1.77
	S3	-2.28	0
	S4	-3.01	0.12
	S5	-2.86	0

* The adsorption height h denotes the vertical distance between Li ion and C_{68}-GY monolayer.

Table 3 The adsorption energy E_{ad}, formation energy E_{form}, and the lattice constant ratios, a/a_0 for Li ions in bilayer C_{68}-GY. The formation energy for these bilayer configurations is calculated by using non-lithiated C_{68}-GY and the lithiated $Li_{1.125}C$ as reference states.

bilayer	$Li_{0.375}C$	$Li_{0.75}C$	$Li_{1.125}C$
E_{ad} (eV)	-0.44	-0.55	-0.43
E_{form} (meV per formula unit)	-3.6	-91.8	0
a/a_0	0.998	0.991	1.032

Table of contents:

A new graphyne with high stability, excellent flexibility and carrier mobility is theoretically predicted as a promising anode material for lithium-ion batteries with high capacity.